E-594

TOTAL CROSS SECTION MEASUREMENTS FOR MUON NEUTRINO AND ANTINEUTRINO CHARGED CURRENT DEEP INELASTIC SCATTERING

by

Terrance Foy Eldridge

B. S., Harvey Mudd College
(1980)

SUBMITTED IN PARTIAL FULFILLMENT
OF THE REQUIREMENTS FOR THE
DEGREE OF

DOCTOR OF PHILOSOPHY

at the

MASSACHUSETTS INSTITUTE OF TECHNOLOGY

JUNE 1985

Signature of Author . . . . . .
Department of Physics, 26 June 1985

Certified by . . . . . .
Thesis Supervisor

Accepted by . . . . . .
Chairman, Department Committee on Theses

To my parents, whose support and encouragement made this possible.

TOTAL CROSS SECTION MEASUREMENTS FOR MUON NEUTRINO AND ANTINEUTRINO CHARGED CURRENT DEEP INELASTIC SCATTERING

by

Terrance Foy Eldridge

Submitted to the Department of Physics
on 26 June 1985, in partial fulfillment of the requirements
for the degree of Doctor of Philosophy.

ABSTRACT

Measurements of the total cross section for muon neutrino and antineutrino charged current events have been made using the fine-grained calorimeter located in Lab C at the Fermi National Accelerator Laboratory. 7919 neutrino and 1520 antineutrino events, after cuts, were obtained from the Narrow Band exposure during the Spring 1982 run. The neutrino energy for each event is obtained by reconstructing the momentum of the exiting muon and the energy of the hadron shower. The cross section slope is given as a function of the neutrino energy; the weighted mean yields a value of $(.613 \pm .007 \pm .031) \times 10^{-38}$ cm^2/GeV for the neutrino cross slope section, and $(.332 \pm .009 \pm .022) \times 10^{-38}$ cm^2/GeV for the antineutrino cross section slope, where the first error is statistical, and the second error contains systematic and scale errors. These measurements are consistent with measurements by previous experiments.

Thesis Supervisor: J. S. Whitaker

Title: Associate Professor of Physics

TABLE OF CONTENTS

LIST OF FIGURES

LIST OF TABLES

CHAPTER I. INTRODUCTION

Shortly after radioactivity was discovered in 1896, Chadwick observed that the electron emitted in beta decay had a continuous spectrum, whereas two body decay kinematics say that the electron should have a fixed energy in the center of mass frame. In order to save conservation of energy and momentum, W. Pauli proposed in 1930 that a neutral particle of near-vanishing or zero rest mass and half integral spin is emitted with the electron. A year later Fermi used Pauli's hypothesis and proposed his own theory of beta decay, calling the new particle a neutrino.

Fifty years later the neutrino is no longer as much a mystery. The Standard Model for electroweak interactions has predicted many new phenomena, some just recently being confirmed by experiments[1]. Why are neutrinos useful for particle physics studies? The answer is at least threefold:

1. There is no electromagnetic or strong force coupling with the neutrino to complicate results.
2. Neutrinos are polarized, hence neutrinos scatter preferentially from quarks and antineutrinos from antiquarks, so the $q\bar{q}$ sea in a nucleon can be studied.
3. The cross section, although tiny (approximately 10^{-38}cm^2), rises linearly with energy, hence rare processes needing higher energies occur more abundantly.

This thesis concerns a measurement of 3) above: the total charged cur-

rent neutrino and antineutrino deep inelastic cross sections. Measurements of these cross sections have been published by many experiments[2,3,4,5,6], some with very high statistics, but the results are still in question — a double-valued quantity at high energy, although narrowed recently, can be found in the literature[7]. It is the goal of this thesis to assist in the understanding of these quantities. In addition to this reason for measuring the total cross section, a result consistent with accepted values lends credibility to further publications from this experiment in more disputed topics of neutrino interactions.

The paper is organized into major sections related to the determination of the total cross section. First, the theoretical equation for the total cross section is given and its underlying assumptions are explained. This is followed by a description of the experimental apparatus and hardware. A section on event reconstruction and analysis is included, along with a summary of the extensive work done on the normalization process. The event Monte Carlos, crucial to acceptance calculations, are explained. The backgrounds and corrections to the final results are described, and the results are given. In finishing, an appendix is included to explain in more detail the method used for determining the muon momentum.

CHAPTER II. THEORY

In the quark-parton model, the differential cross section for neutrino (antineutrino) charged current scattering from stationary nucleons is given by[8]

$$\frac{d^2\sigma_\nu^\rho}{dx\,dy} = \frac{G^2 M E_\nu}{\pi}\left[[1+(1-y)^2]F_2(x) \mp [1-(1-y)^2]xF_3(x)\right], \qquad (2.1)$$

where M is the nucleon mass, and

$$Q^2 = -q^2 = -(P_\nu - P_\mu)^2, \qquad (2.2)$$

$$\nu = E_\nu - E_\mu, \qquad (2.3)$$

$$x = \frac{Q^2}{2M\nu}, \qquad (2.4)$$

$$y = \frac{\nu}{E_\nu}. \qquad (2.5)$$

See Figure 2.1. G is the weak coupling constant, and $F_2(x)$ and $xF_3(x)$ are nucleon structure functions.

Various assumptions and approximations have been made to arrive at this result. Due to the finite mass of the W boson propagator a factor $(1+Q^2/M_W^2)^{-2}$ is introduced, but has been neglected because of the relative magnitude of M_W^2 compared to the mean value of Q^2 in this experiment:

$$\langle Q^2\rangle \simeq 13\text{GeV}^2, \quad M_W^2 \simeq 6500\text{GeV}^2.$$

Three other structure functions have been neglected because they enter with terms of order m_μ/E_ν. In addition, the Callan-Gross relation has

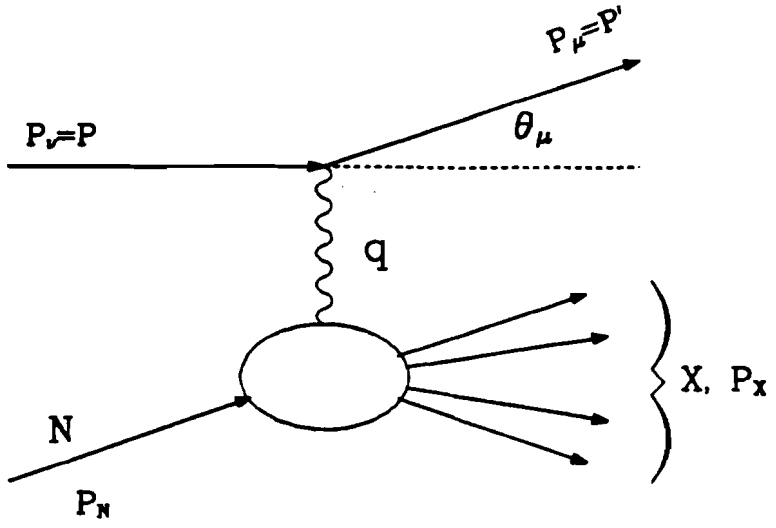

Figure 2.1. Neutrino charged current deep inelastic scattering from a nucleon.

been applied, which specifies that because the quarks are spin 1/2 and have negligible tranverse momentum in the nucleus

$$2xF_1(x) = F_2(x). \tag{2.6}$$

Bjorken scaling is also assumed, yielding structure functions that are independent of Q^2, i.e.

$$F_i(x, Q^2) \rightarrow F_i(x). \tag{2.7}$$

This assumption, which implies that the structure functions are independent of any mass scale, arises from the pointlike behavior of the constituents within the nucleon.

QCD effects[9], which can also break the scaling of the structure functions, are also ignored in Equation (2.1). These show up in the Q^2 evolution of the structure functions due to the emission of gluons. There is also a contribution

from higher twist effects, a condition where the interaction is not with a quasi-free quark. These QCD effects have been included in the Monte Carlo event generation.

The physical meanings of the two structure functions $F_2(x)$ and $xF_3(x)$ are related to the quark densities within an isoscalar nucleon by

$$F_2(x) = x[q(x) + \bar{q}(x)], \tag{2.8}$$

$$xF_3(x) = x[q(x) - \bar{q}(x)], \tag{2.9}$$

where

$$q(x) = u(x) + d(x), \tag{2.10}$$

$$\bar{q}(x) = \bar{u}(x) + \bar{d}(x), \tag{2.11}$$

and where $u(x)$ and $d(x)$ are the densities of the u and d quarks, and $\bar{u}(x)$ and $\bar{d}(x)$ are the densities of the antiquarks, respectively, as a function of x. Contributions from heavier quarks have been neglected. In these equations x can be thought of as the fraction of nucleon momentum carried by the quark, a statement completely equivalent to Equation (2.4). In addition, the structure function $xF_3(x)$ can be shown to be proportional to $\sigma_R - \sigma_L$, the right- and left-handed 'W absorption cross sections' for the interaction. Since the W transmits the parity non-conserving weak interaction, this term violates parity conservation and is therefore missing in the electromagnetic scattering cross section.

There are no good theoretical predictions for the structure functions. However, Regge pole analysis[10] and the Drell-Yan process[11] suggest that the valence quarks are described by

$$q(x) - \bar{q}(x) = A\sqrt{x}(1-x)^n, \tag{2.12}$$

while 'counting rules'[12] give

$$q(x) = B(1-x)^m. \tag{2.13}$$

CDHS, a neutrino experiment at CERN, has measured n and m to be[13]

$$n = 3.5 \pm 0.5, \tag{2.14}$$

$$m = 6.5 \pm 0.5, \tag{2.15}$$

and has determined

$$\int_0^1 F_2(x)\,dx = 0.45 \pm 0.03. \tag{2.16}$$

In addition, the Gross-Llewellyn Smith sum rule[14] predicts

$$\int_0^1 F_3(x)\,dx = 3. \tag{2.17}$$

Given Equations (2.14)–(2.17) the constants A and B can be determined so that a functional form of the structure functions can be expressed. This is used in the event generating Monte Carlos for estimation of errors due to the uncertainty in the knowledge of the structure functions, to be discussed later.

If Equation (2.1) is integrated over x and y we get the total cross section:

$$\sigma_\nu^p(E_\nu) = KE_\nu, \tag{2.18}$$

where K is some constant. Equation (2.18) predicts that the total cross section, under the assumptions mentioned earlier, is a linear function of E_ν.

The total cross section can be written in terms of experimentally measurable quantities as

$$\sigma_T(E_\nu) = \frac{N_e(E_\nu)}{\varepsilon A(E_\nu)} \frac{1}{N_\nu(E_\nu)} \frac{a_{fid}}{N_N} C_I, \tag{2.19}$$

where

$N_e(E_\nu) \equiv$ Number of neutrino events after cuts

$\epsilon \equiv$ reconstruction efficiency

$A(E_\nu) \equiv$ acceptance

$N_\nu(E_\nu) \equiv$ number of incident neutrinos

$a_{fid} \equiv$ fiducial area

$N_N \equiv$ number of nucleons within the fiducial volume

$C_I \equiv$ isoscalar correction

A word should be said about C_I. The theoretical total cross section assumes an isoscalar target — a target with equal numbers of protons and neutrons. Since our target does not satisfy this then a correction must be made. What we measure is

$$\sigma_{\text{meas}} = \frac{N_p\sigma_p + N_n\sigma_n}{N_p + N_n}, \tag{2.20}$$

and what we want to determine is the total cross section for an isoscalar target:

$$\sigma_T = \frac{1}{2}(\sigma_p + \sigma_n). \tag{2.21}$$

If we let

$$R_I = \sigma_p/\sigma_n, \tag{2.22}$$

$$I = \frac{N_p - N_n}{N_p + N_n}, \tag{2.23}$$

then we can write

$$\sigma_T = \sigma_{meas}\left[\frac{1 + R_I}{(1 + I)(R_I - 1) + 2}\right]. \tag{2.24}$$

So the isoscalar correction, C_I, is

$$C_I = \frac{1 + R_I}{(1 + I)(R_I - 1) + 2}. \tag{2.25}$$

Experiments[15,16] have measured R_I to be

$$R_I = .48 \pm .02 \pm .05 \quad \text{for neutrinos,} \tag{2.26}$$

$$R_I = 1.96 \pm .04 \pm .12 \quad \text{for antineutrinos,} \tag{2.27}$$

where the first error is statistical and the second is systematic. I for our detector has been calculated to be

$$I = -.022 \pm .002. \tag{2.28}$$

hence

$$C_I = .9924 \pm .0013 \quad \text{for neutrinos,} \tag{2.29}$$

$$C_I = 1.0072 \pm .0009 \quad \text{for antineutrinos.} \tag{2.30}$$

CHAPTER III. EXPERIMENTAL APPARATUS

3.1 Accelerator

The experiment was performed at the Fermi National Accelerator Laboratory (Fermilab) in Batavia, Illinois. Fermilab is a high energy physics laboratory, and contains a proton accelerator which during the run (January 1982 - June 1982) was operated at the maximum operating energy of 400 GeV. The protons were extracted from the Main Ring approximately every 15 seconds. The spill was split into two divisions: slow spill, where the extraction took place over approximately 1 second, and fast spill, which was at the tail end of the slow spill and lasted about 1 millisecond. The detector, located at Lab C, was gated live only during the fast spill in order to reduce the dead time from false triggers due to cosmic rays. See Figure 3.1 for the location of Lab C with respect to the accelerator and beam lines, and Figure 3.2 for the neutrino beam line.

Protons destined for the neutrino line are transported to Target Hall where they are focused onto a beryllium oxide target. Secondary particles emerging from the target are primarily p's, K's, π's, μ's, and e's with a small number of other particles. Immediately following the target is the 'train', a series of bending and focusing magnets which are on a train-like assembly and is rolled into place on a track; see Figure 3.3. The train follows a gentle corkscrew shape, from which exiting particles head directly down the neutrino beam line in the decay pipe towards Lab C. The corkscrew shape is

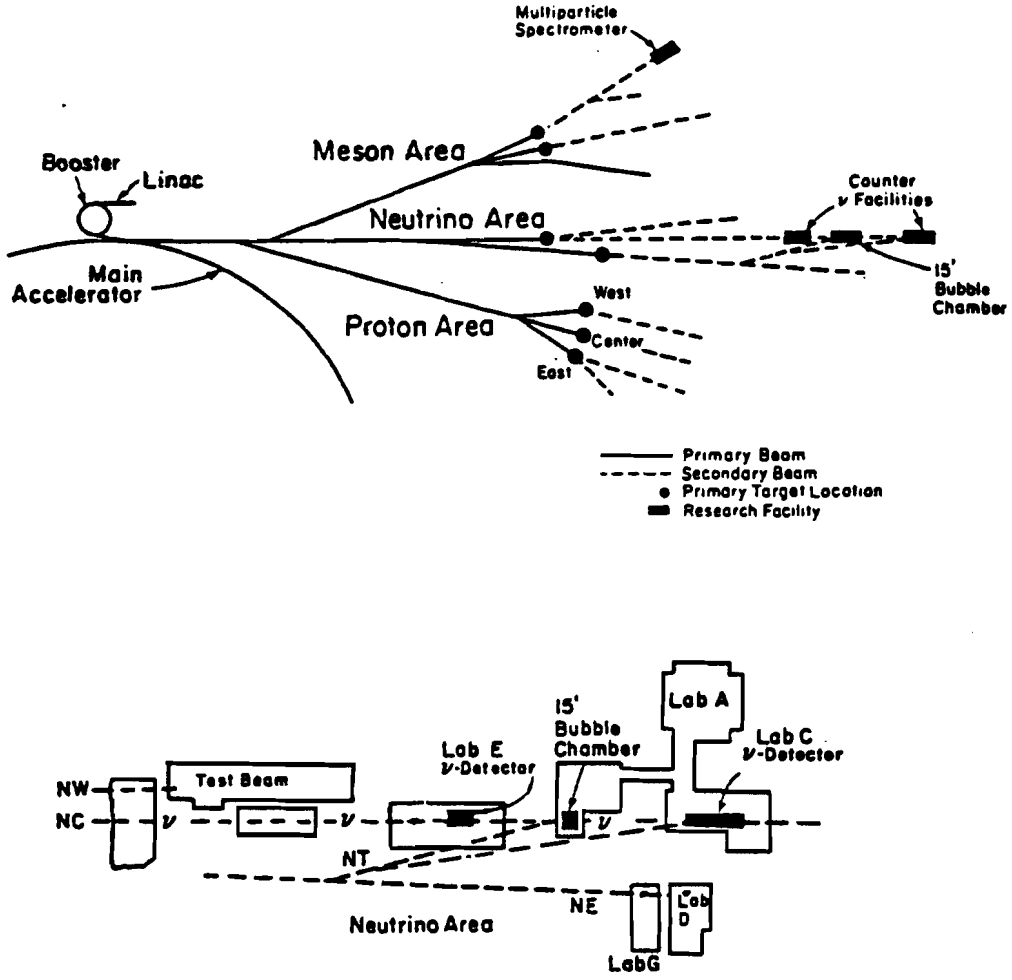

Figure 3.1. Fermilab beam lines and the location of Lab C.

intended to direct decays occuring within the train away from Lab C. The train magnets are set to a specific value to give the secondaries a known momenta and a specific momentum 'bite', chosen to be 10%. This configuration is known as a 'narrow band beam' because the momentum spread of the secondaries is so narrow; contrast this to a 'wide band beam' where the secondaries are collected off the target and focused without regard to momentum. The narrow band beam is useful because the neutrino energy is correlated to the radial distance of the event vertex from the beam line.

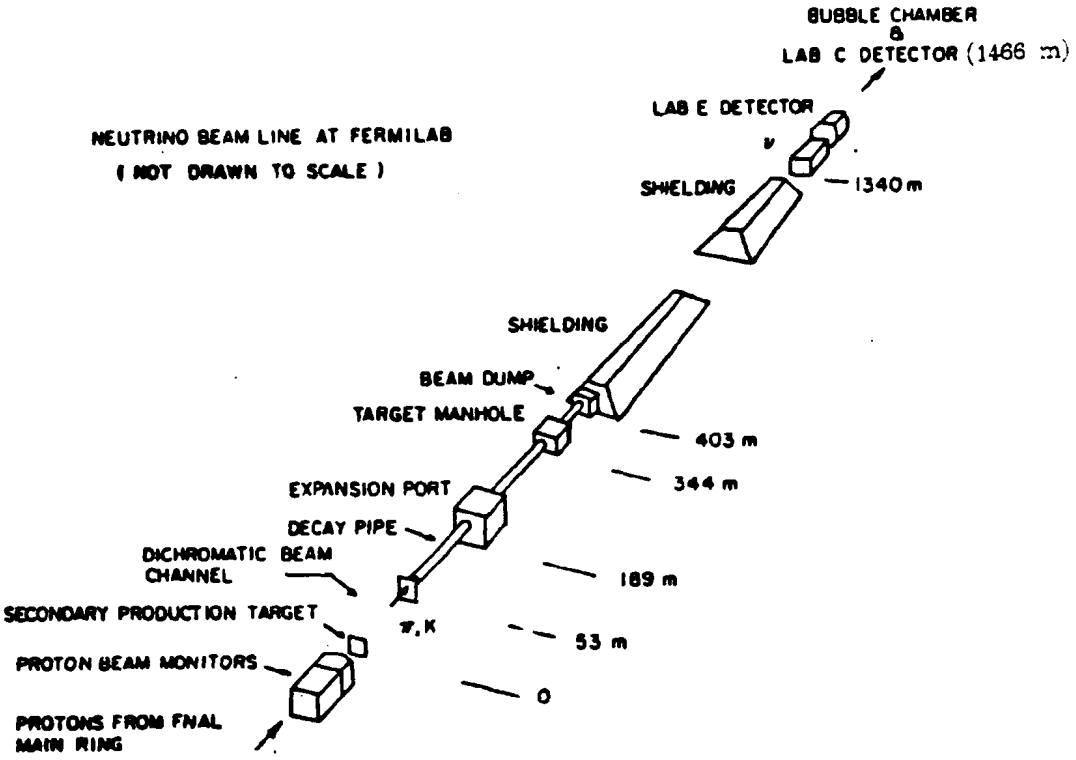

Figure 3.2. Fermilab neutrino beam line.

This correlation will be discussed in detail later.

Neutrinos produced in this beam line are generated from the decays of the secondaries. Prompt decays from the heavier mesons occur immediately after the target. Because the primary beam is directed away from Lab C, and the number of these mesons is small, the number of neutrinos arriving at Lab C from this reaction is many times smaller than the number of neutrinos from momentum-selected decays.

Secondaries that have traversed the train are composed primarily of protons, electrons, muons, pions, and kaons. Protons and electrons do not decay. Muons decay, but because the number of muons is extremely small, and the lifetime is relatively long, the number of neutrinos from this decay can be ignored. This leaves only the π's and K's. The principle decay modes

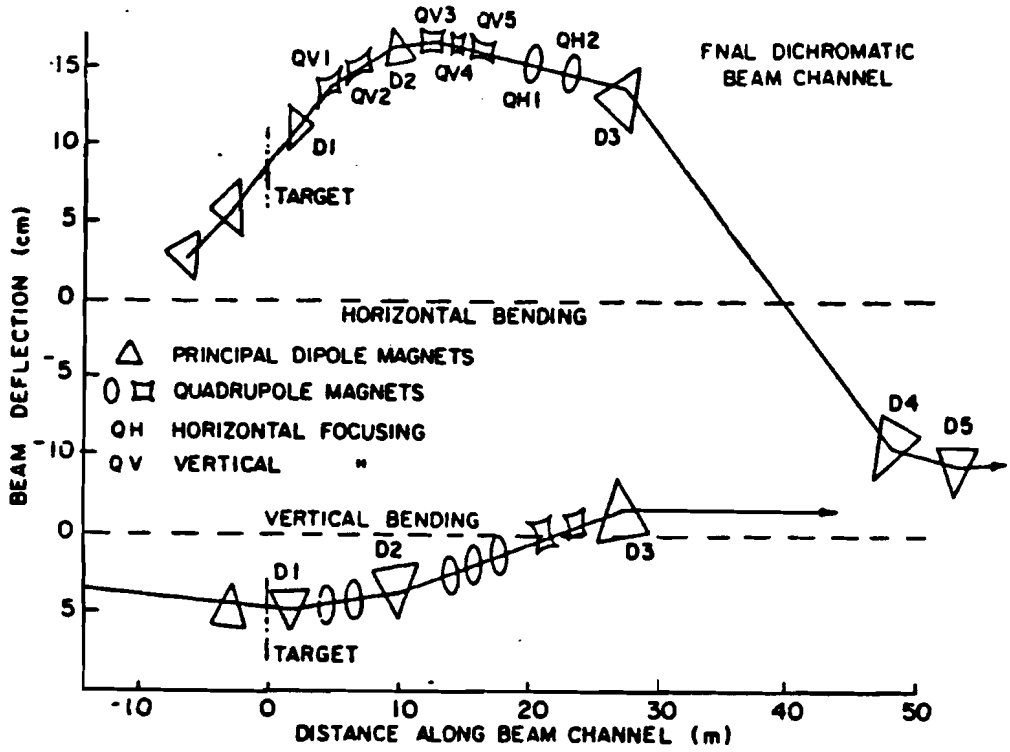

Figure 3.3. Schematic diagram of the dichromatic magnet train.

are:

$$\pi \rightarrow \mu + \nu_\mu \qquad \text{BR=100\%}$$

$$K \rightarrow \mu + \nu_\mu \qquad \text{BR=63.51\%}$$

$$K \rightarrow \pi + \mu + \nu_\mu \qquad \text{BR=3.18\%}$$

$$K \rightarrow \pi + e + \nu_e \qquad \text{BR=4.82\%}$$

The last three-body decay produces an electron neutrino, and hence cannot contribute to the final event sample. The two-body decays have an energy-radius correlation: at a given radius in the Lab C detector each two-body reaction has its own characteristic energy, smeared by the location of the decay in the decay pipe and the momentum bite. The three-body reaction from the K decay has no such relationship. A Monte Carlo scatter plot of the two- and three-body decay events in the detector are shown in Figure 3.4.

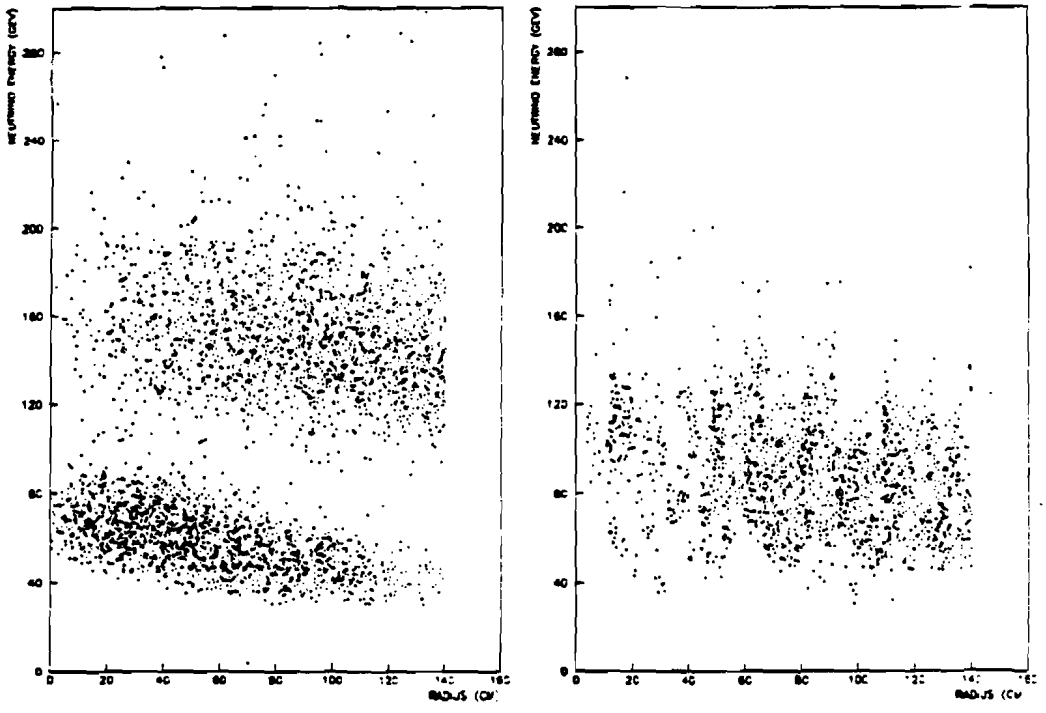

Figure 3.4. Monte Carlo energy-radius scatter plots of the event vertex for the various decay modes. The left plot shows the two-body decays from the π and K secondaries, and the right plot is from the three-body $K_{\mu 3}$ decay.

Not all decays are produced in the decay pipe after the hadrons are momentum selected, unfortunately. Decays also occur in the train which contribute to an energy dependent background. The corkscrew shape of the train is an attempt to minimize this background by keeping the trajectory of the secondaries pointed away from the detector for as long as possible. A spectrum of this background for the +165 GeV/c train setting is shown along with the signal in Figure 3.5.

Monitors are located at various points along the beamline to detect and quantify both the primary and secondary beams; see Figure 3.6. Upstream of

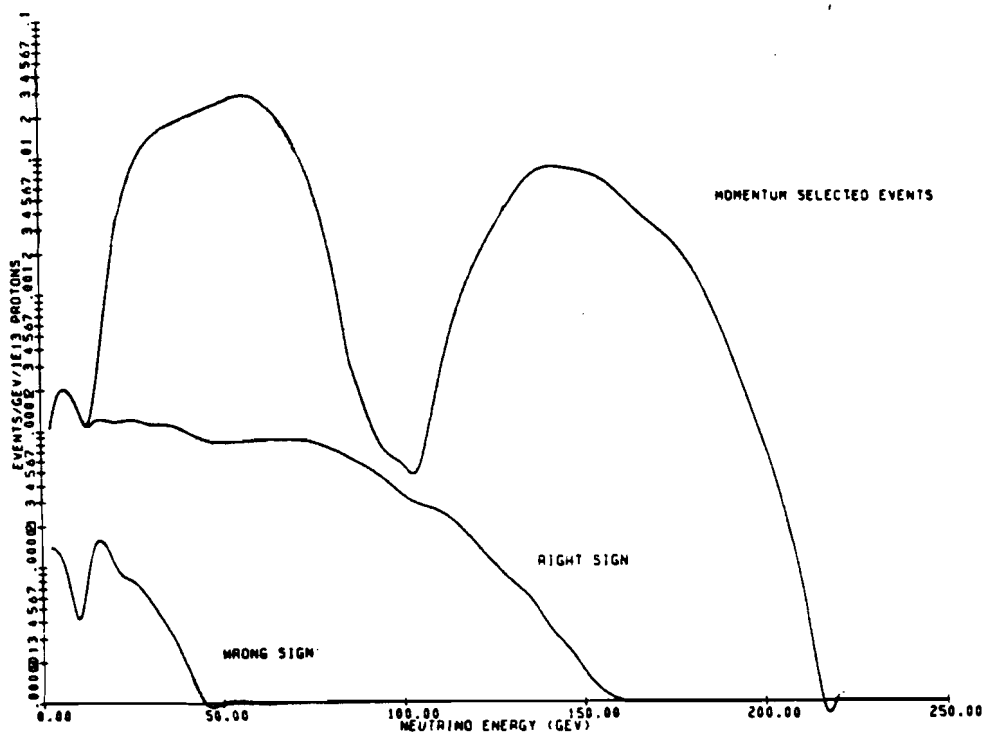

Figure 3.5. Monte Carlo narrow band signal and wide band background for +165 GeV train. The right sign background contributes to the neutrinos, the wrong sign to the antineutrinos.

the target is located N0TOR, a toroid that converts the changing magnetic field from the beam current pulse to a voltage pulse. Logical device NT digitizes and scales this voltage, thus producing a measurement of the proton flux.

Downstream of the train is the Expansion Port which houses a Čerenkov counter, an RF cavity, two ion chambers (one enclosing a split plate gap), and a SWIC.

An ion chamber is a device which enables the number of charged particles in a beam to be measured; the 'U' ion chamber is shown in Figure 3.7 — chambers 'I' and 'M' are similar in operation, except both include split plate

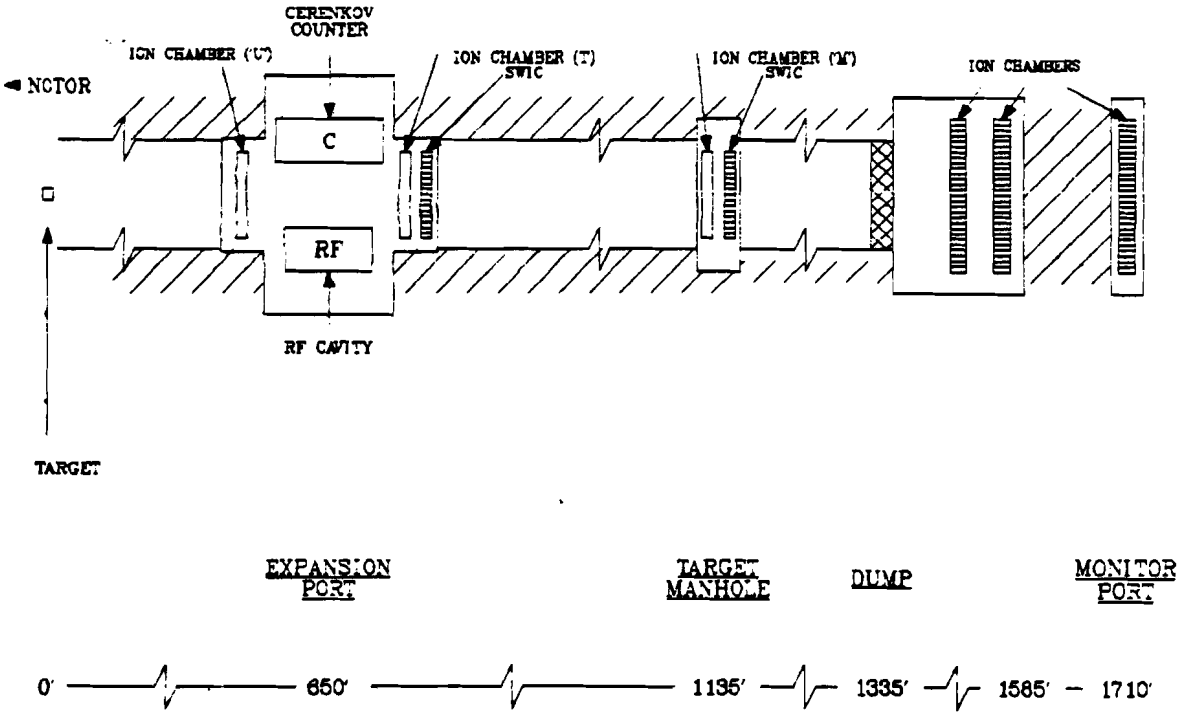

Figure 3.6. Location of monitors within the flux monitoring system.

gaps. An ion chamber operates with unity gain as opposed to proportional tubes, for example, which produce charge multiplication at the anode. The chambers are filled with helium at atmospheric pressure, so that a charged particle traversing the chamber leaves a trail of ionized gas. A thin foil provides a low impedance to ground and collects the free electrons, yielding a total charge that is a function of the number and type of particles passing through the chamber. The split plate gap is similar to having two ion chambers side-by-side with the seam in the center of the chamber, and is used for monitoring the beam location by calculating the relative fraction of energy deposited in the two halves. The chambers also include a 'source gap', a gap within the chamber that contains a 70 μcurie source of Americium to provide a constant monitoring of the chambers and the subsequent electronics.

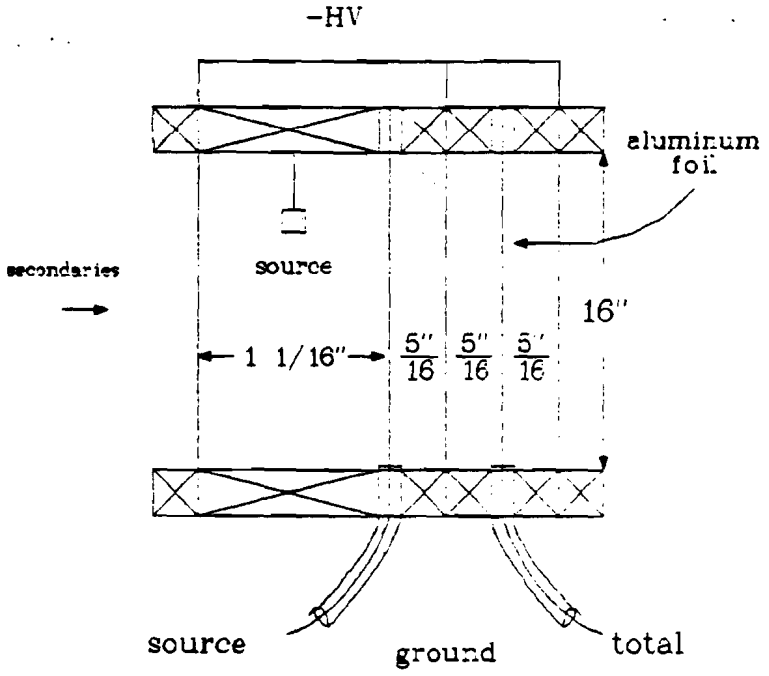

Figure 3.7. Cross-sectional view of the cylindrical 'U' ion chamber. The windows are made of .002" aluminized mylar, and the foils between the chambers are .0015" aluminum; the other ion chambers are similar in design, but enclose split plate gaps.

The Čerenkov counter and RF cavity are on a motorized moveable table so that only one is in the beam at a time. The normal operating condition is to have the RF cavity in the beam, while the Čerenkov cavity is rolled in periodically to determine beam compositon. A schematic of the RF cavity is shown in Figure 3.8. The RF cavity operates by taking advantage of the 53.1 Mhz structure of the beam to produce a voltage that is a function of the amount of total charge (a π^+ and a π^- together, for example, would produce no signal).

A SWIC, Segmented Wire Ion Chamber, is a device which has many parallel, planar wires used for determining the beam location and profile.

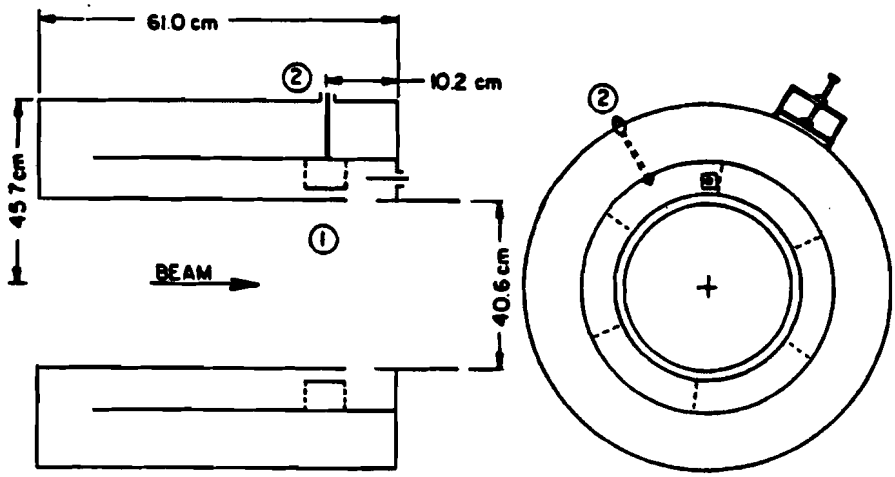

Figure 3.8. Schematic of the RF cavity. The cavity is a folded 20 ohm coaxial transmission line, with one end shorted to form a quarter wave resonator, constructed of pure aluminum. (1) is the gap excited by the rf structure of the beam; (2) is a magnetic loop tap.

Continuing downstream from the Expansion Port is the Target Manhole. In this enclosure is an ion chamber (housing a split plate gap), and SWIC. Further downstream is the berm, a long mound composed of earth, iron, and concrete used to filter out muons from secondary decays and the secondaries that have not decayed. Chambers were placed within the berm for muon flux identification, but were not used for the analysis.

3.2 E594 Detector

3.2.1 Construction

A schematic of the E594 detector is shown in Figure 3.9. The detector is composed of a target-calorimeter section which provides the energy determination of the hadron shower from the neutrino interaction. This section is constructed with proportional planes and flash chambers, and sand and steel

shot to provide a target material. Downstream is the muon spectrometer, composed of iron toroid magnets and proportional planes used for calculating the momentum of the muon exiting from the interaction.

An absolute necessity for a neutrino experiment is a significant target mass because of the extremely small neutrino cross section. The total mass of the calorimeter is 340 tons, while the fiducial mass used for this analysis is 100 tons. The primary target material in the calorimeter is a series of planes of plastic extrusions filled with sand or steel shot, giving a radiation length of 13 cm, an absorption length of 97 cm, and a density of 1.3 g/cm^3.

A detector must be triggerable with enough pattern recognition capability to reject noise and unwanted events. This requirement is satisfied by 37 proportional planes.

The proportional planes are spaced equally within the detector, with each odd (even) plane sampling the vertical (horizontal) view. Each plane is 12 ft by 12 ft, composed of 18 aluminum extrusions. Each extrusion contains 8 cells, a cell measuring .840 in by .910 in and enclosing a 50 micron gold-plated tungsten wire strung down the center. The wires in neighboring cells are spaced 1 in apart. A gas mixture of 90% argon and 10% methane flowed continuously through the plane at a rate of .5 CFH, and 1650 Volts was applied on the wires. Calibration of the planes was done by placing cadmium (Cd) sources over each wire, and every spill a calibration cycle read out the pulse heights from the Cd decays. The rate from the Cd sources was 1 kHz per plane, yielding a negligible background to the triggered event.

Signals from the prop plane wires are read out such that four neighboring wires are ganged together, i.e. wires 1, 2, 3, and 4 become channel 1, wires 5, 6, 7, and 8 become channel 2, etc., reducing the number of signals from 144 to 36 and worsening the spatial resolution to approximately $\frac{4\,in}{\sqrt{12}}$. Each of

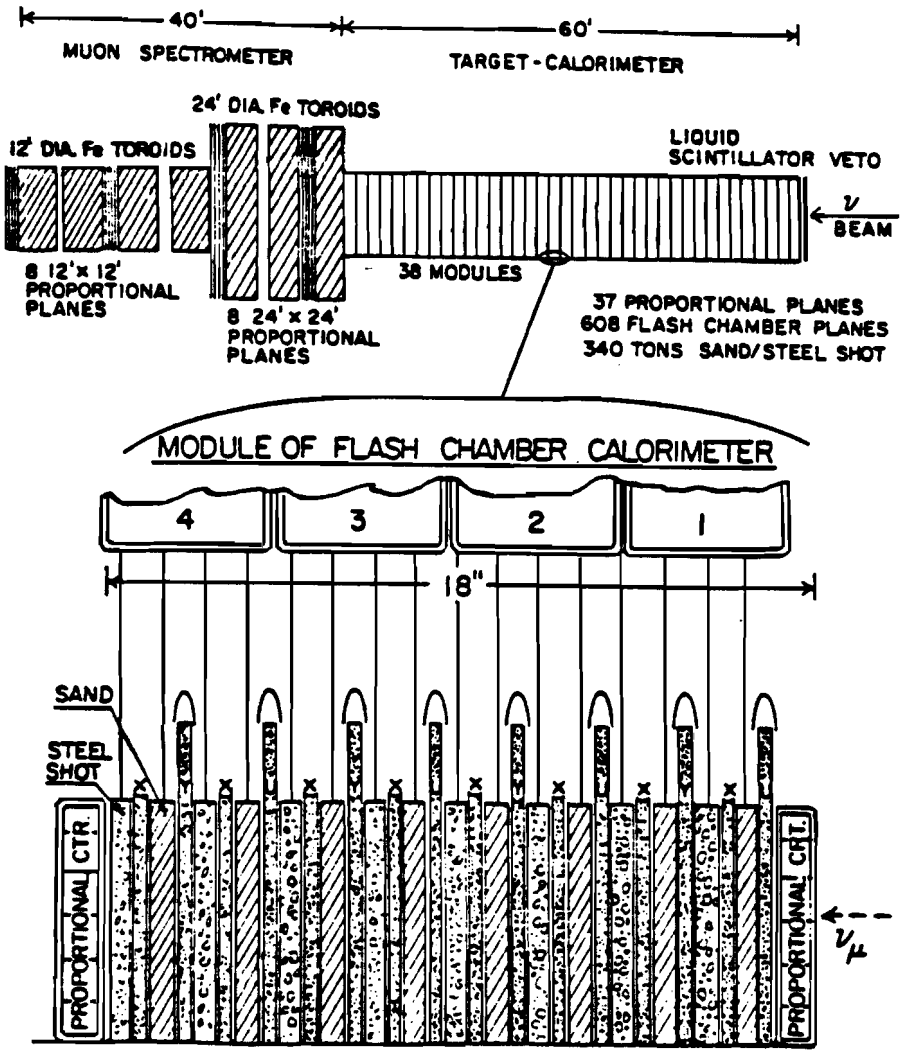

Figure 3.9. E594 detector.

the 36 channels is amplified, and this signal processed to produce a 'fast out' (FO), a pulse designed to bring out the signal quickly for triggering purposes, and a 'slow out' (SO), a sample-and-hold stage for integrating the charge on the wire, used for off line pulse height analysis; see Figure 3.10. The fast out for each channel is summed to produce a 'sum out' (Σ), the signal sent to the triggering logic, and is also processed further on the plane to give an analog multiplicity (AM), a signal whose amplitude is proportional to the number of wires struck. The sum out is a measure of the amount of energy deposited

in the plane, and the AM is used for determining the width of the shower in the plane. The fast outs are also latched on the plane to be read out as a 'hit bit' (HB), a logical signal simply denoting whether the wire was hit or not for off line analysis.

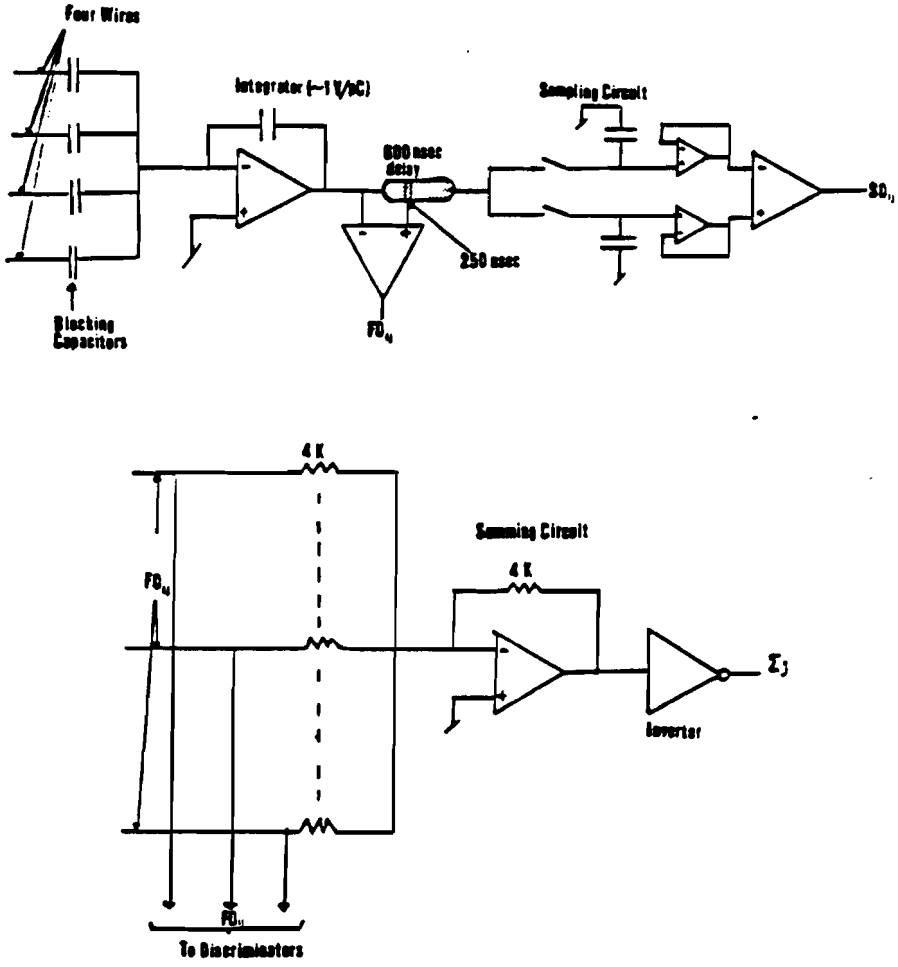

Figure 3.10. Proportional tube readout scheme.

The spatial resolution of the proportional planes, as mentioned earlier, is poor and insufficient for event identification and reconstruction. Instead, the identification and reconstruction is performed using the fine granularity of the flash chambers, which have a much better resolution, but are pulsed

devices, *i.e.* they cannot trigger themselves. In addition, the number of cells hit in the flash chambers determine the energy of the hadron shower.

There are 608 flash chambers in the detector, arranged in U-X-Y-X modules, the X view sampling vertically, and the U and Y views sampling ±10 degrees off horizontal. Each chamber is made from extruded polypropylene, and resembles cardboard, having cell sizes of 5.0 mm by 5.9 mm. A 90% neon-10% helium gas mixture, with some trace contaminants purposely added, is flushed constantly through the chambers. The contaminants are added to prevent refiring since a clearing field is not applied between pulses.

Each flash chamber has a sheet of .005 in aluminum foil glued to each side, with one side held at ground. When a decision is made that this event is to be 'flashed' a 5 KV pulse is applied to the opposing side. For each cell that a charged particle has traversed, the electric field creates a plasma discharge which propagates down the cell. The pulse is read out by magnetostrictive wire techniques. Because the flash chamber high voltage system must recharge, only one event per spill can be recorded.

Downstream of the calorimeter is the muon spectrometer, designed to measure the momentum of muons from the charged current interactions. A series of toroid magnets operated at approximately 20 KG provides the bending. The first three toroids are 24 ft in diameter, each 60 cm thick and composed of three slabs, and the following four toroids are 12 ft in diameter, each being 125 cm thick and composed of six slabs. Each 24 ft toroid has a 2 ft diameter bore in the center to allow room for the coils, and each 12 ft toroid has a 1 ft diameter bore. Field measurements of the 24 ft and 12 ft magnets were taken using a Hall probe inserted into gaps in the magnets. These measurements are plotted in Figures 3.11 and 3.12. Using POISSON[17] this field and the field within the iron can be determined from

the magnet structure and its permeability. POISSON results agreed with the measurements, although due to poor construction of the 24 ft magnets the field within different slabs exhibit quite a spread in values, as seen in Figure 3.11. Figures 3.13 and 3.14 show the field values within the iron used for momentum analysis as determined from POISSON.

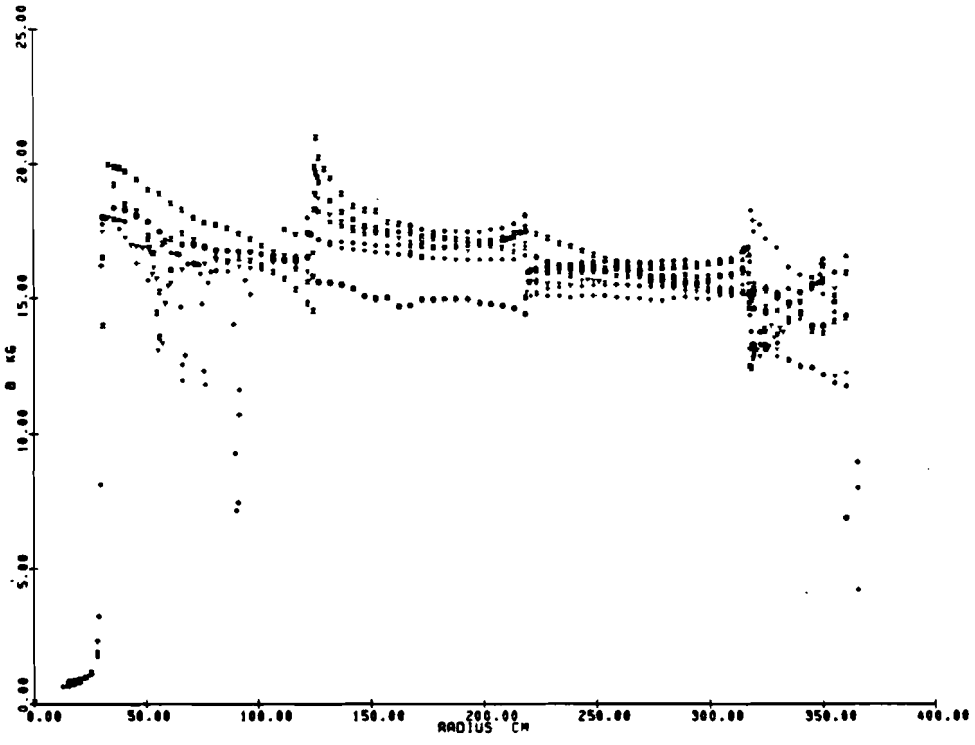

Figure 3.11. Field measurements within slots in the different slabs of the 24 foot diameter toroid magnets. The different points are the different slabs, and the sudden transitions as a function of radius are due to the layered construction of the magnets.

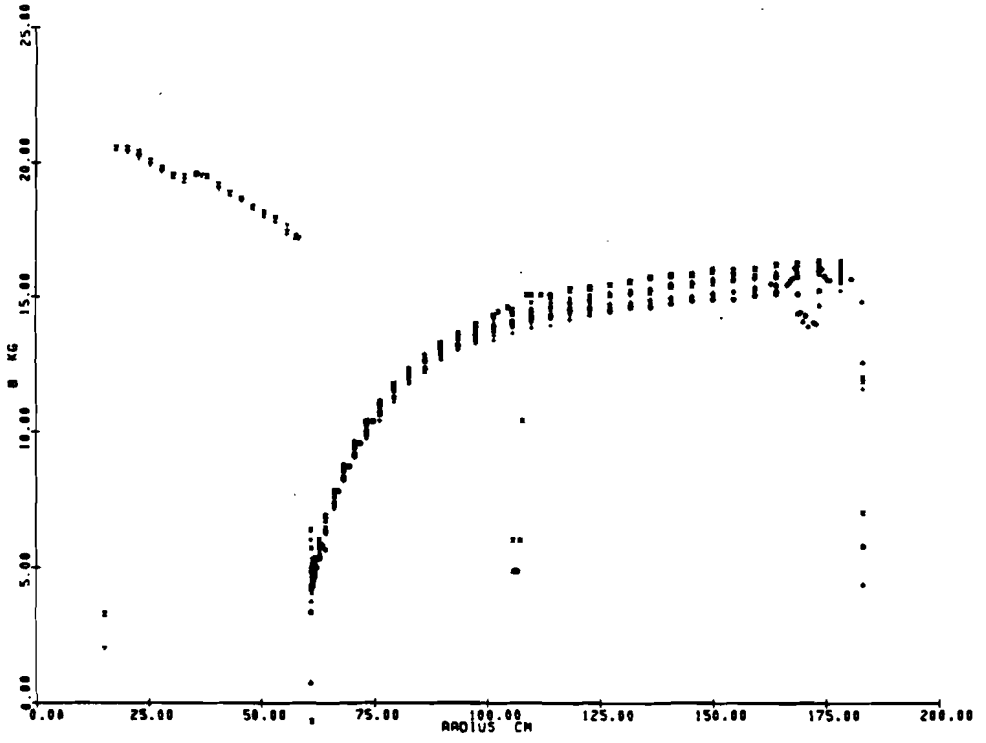

Figure 3.12. Field measurements within slots in the different slabs of the 12 foot diameter toroid magnets. The dip at ≈60 cm occurs because the slot used for measurements is not radial.

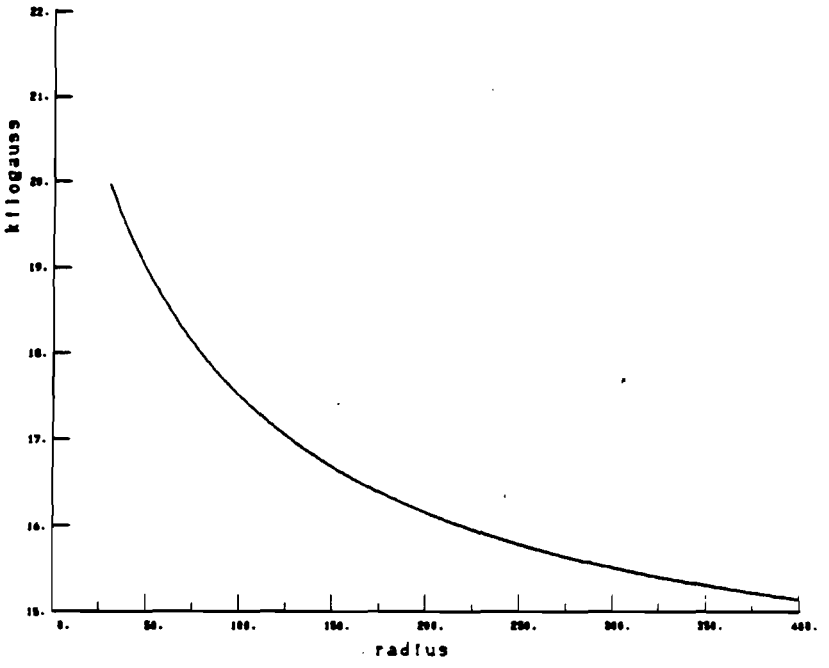

Figure 3.13. Field values for the 24 ft toroids used for momentum analysis. Note the ordinate axis is zero-suppressed.

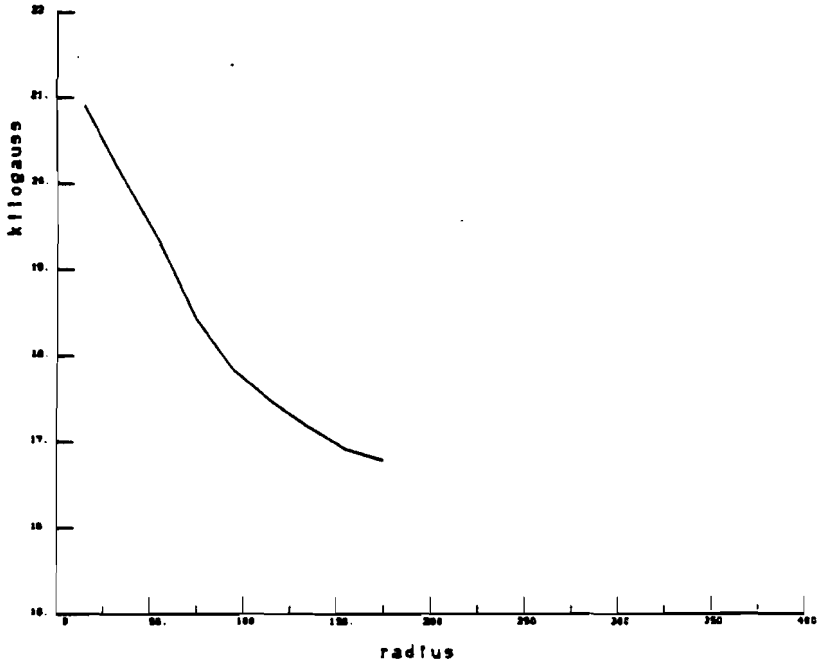

Figure 3.14. Field values for the 12 ft toroids used for momentum analysis. Note the ordinate axis is zero-suppressed.

Four of the toroid gaps were instrumented with proportional chambers sampling both vertical and horizontal coordinates. The first two instrumented gaps contain planes constructed in the shape of a 'cross' to adequately cover the area of the 24 ft toroids, and the planes in the latter two gaps were of the same dimension as the calorimeter proportional planes, 12 ft by 12 ft. Each toroid proportional plane was double sided with opposing sides having their wires offset by half a cell. The planes were read out with resistive charge division: 8 wires (16 in the first gap) were attached to each other with resistors and the pulse height from the two ends was read out; see Figure 3.15. Calculating the delta,

$$\delta = \frac{\text{pulse height from end 1} - \text{pulse height from end 2}}{\text{pulse height from end 1} + \text{pulse height from end 2}}, \qquad (3.1)$$

for an 8-wire (16-wire) section determines in which cell the particle traversed. This method averages tracks from one 8-wire (16-wire) gang into one wire. A histogram of the delta over many events of one 8-wire charge divison section is shown in Figure 3.16. The 8-wire charge division yields a spatial resolution of approximately 1.5 cm, and the 16-wire charge division has a resolution of twice that. This resolution has been determined by a distribution of hit positions in one face of a toroid plane given a hit has occured in the opposing face, and is larger than what one would expect ($\frac{1\text{in}}{\sqrt{12}}$) because of delta rays shifting the center of the charge deposition. Each toroid proportional plane triggered itself for each event when enabled by a pretrigger generated by the calorimeter proportional planes.

Energy resolutions were determined from a hadron or muon calibration beam at nominal settings of 20, 40, 70, and 100 GeV. It turns out that the muon momentum resolution depends on the muon track geometry: muons traveling near the toroid bore or edges have a poorer resolution than those that stay completely in iron. For this reason the muon for each event is

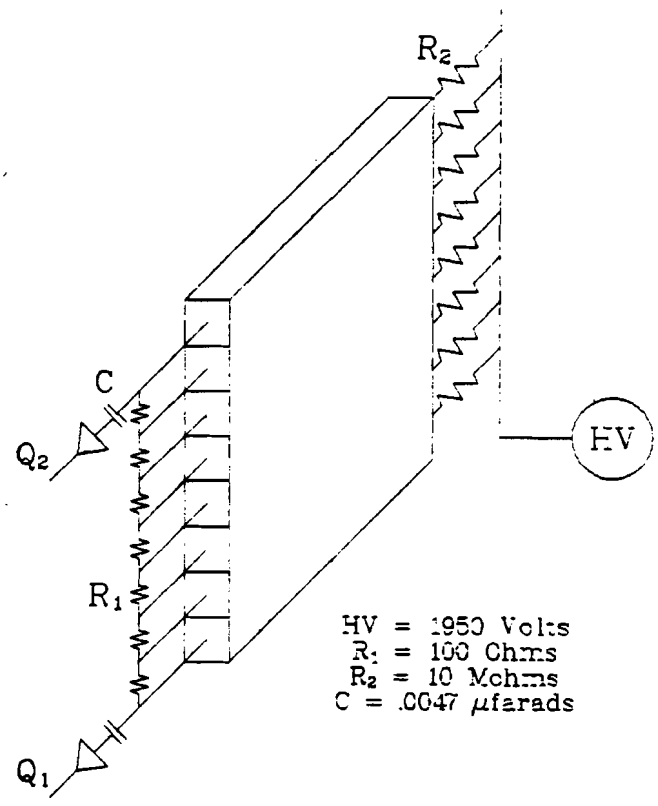

Figure 3.15. 8-wire resistive charge division applied to a toroid proportional plane.

classified depending on its trajectory. If the muon, as predicted from the fitting program, stays away from the bore and the outside edge of the magnet everywhere, then the muon is defined to be class '0'. If the muon crosses the bore or approaches the edge of the magnets (but stays inside) then it is defined to be class '1'. The calibration muons taken do not (except for one momentum setting) approach the hole or edge, hence the resolutions for muons of class '1' must be determined from the shower event Monte Carlo (see Chapter 6). Hadron shower energy calibrations are discussed in more detail in Chapter 8.3. The energy resolutions are given in Table 3.1, and the hadron energy resolutions from the calibration beam are shown in Figure

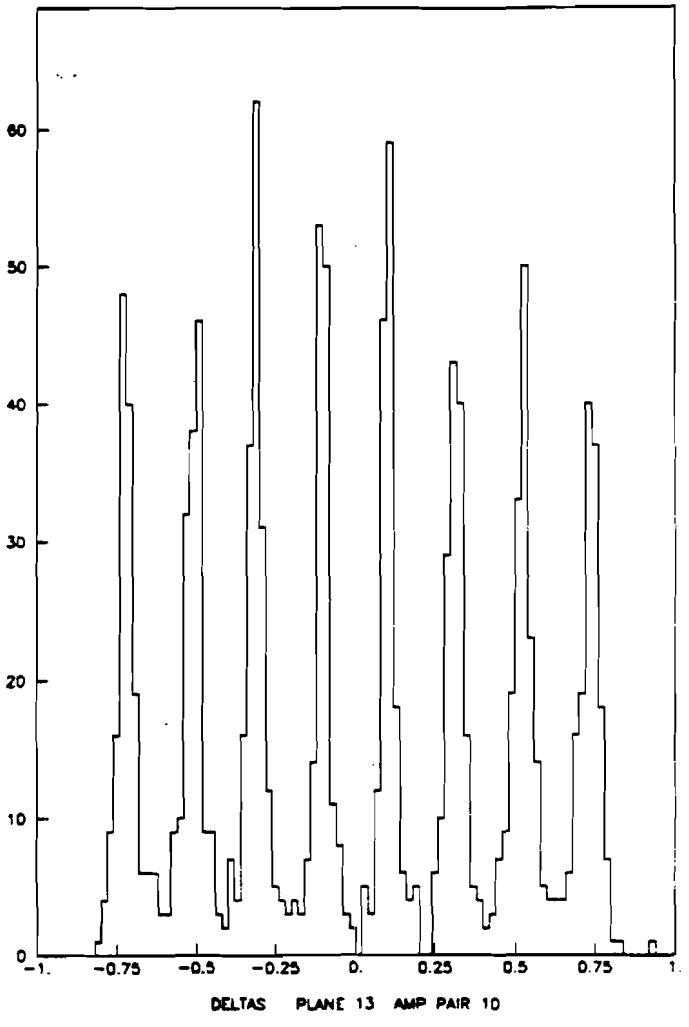

Figure 3.16. Histogram of the delta (Equation (3.1)) over many events from one 8-wire charge division section as diagrammed in Figure 3.15.

3.17. A fit of the hadron energy resolution is made to the form

$$\frac{\Delta E}{E} = C_1 + \frac{C_2}{\sqrt{E}}, \tag{3.2}$$

where C_1 and C_2 are the parameters of the fit, because the energy of the shower is proportional to the total track length of all the shower particles, and the error of the length follows a $\frac{1}{\sqrt{E}}$ distribution. The constant term is included to account for the saturation of the flash chambers at high energy.

$$\textit{hadron energy:} \quad \frac{\Delta E}{E} = .052 + \frac{.519}{\sqrt{E}}$$

$$\textit{muon momentum (0):} \quad \frac{\Delta P}{P} = \sqrt{.0081 + 6.9 \times 10^{-7} P^2}$$

$$\textit{muon momentum (1):} \quad \frac{\Delta P}{P} = \sqrt{.013 + 8.6 \times 10^{-6} P^2}$$

Table 3.1. Energy resolutions. The hadron energy and class '0' muon momentum resolutions were determined from a calibration beam. Class '1' muon momentum was found from Monte Carlo. Refer to the text for a discussion of muon classes.

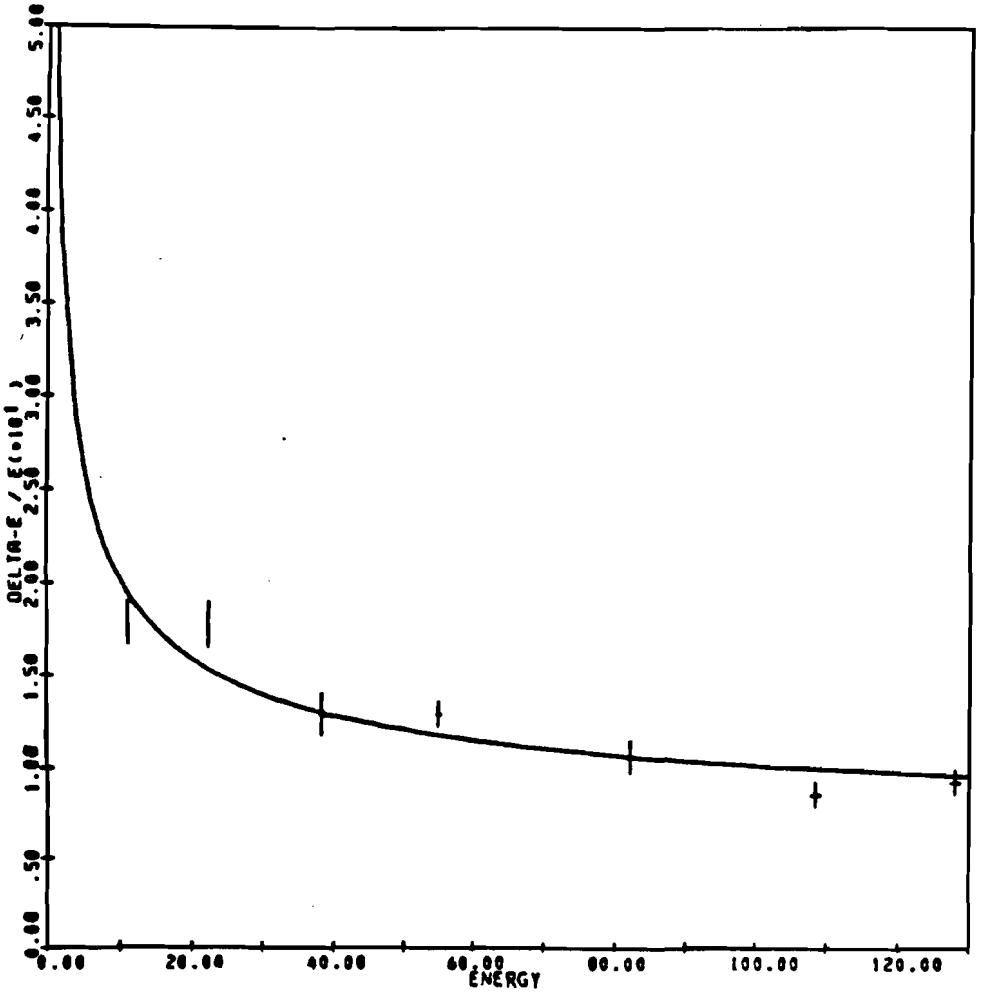

Figure 3.17. Resolutions from the hadron calibration beam. Included is a ($\frac{1}{\sqrt{E}}$+constant) parameterisation, given in Table 3.1.

In order to veto the event trigger on muons produced from upstream

neutrino interactions, a liquid scintillator counter was placed at the front of the detector. Scintillator counters were also placed at eight locations throughout the detector to be used for interspill triggering, but they were never used for triggering a neutrino event.

3.2.2 Triggers and Data Acquisition

There were two competing triggers which were enabled during the accelerator spill and are labeled QUASI and PTH.

The QUASI trigger is intended to identify quasi-elastic events, an event characterized by little or no hadron energy and a muon traveling nearly straight ahead. The trigger used was $BG \cdot \bar{A} \cdot M \cdot F \cdot B$, where BG is the beam gate (a dynamic gate generated by N0TOR when the beam intensity was above a minimal value), A is the anti-counter (the first scintillator; see Figure 3.9), M is a coincidence of at least two proportional planes' discriminated sumout, and F and B are logical OR's from the front and back 12 ft toroid proportional planes. This trigger should pick up events with a muon independent of hadron energy.

The PTH trigger is designed to identify all events that have a minimal hadron energy deposition. The trigger was $BG \cdot \bar{A} \cdot M \cdot AM(>1,>1) \cdot \sum\sum 75$. The quantity $AM(>1,>1)$ is true when the analog multiplicity shows more than one plane to have more than one channel hit, and $\sum\sum 75$ is the 'sumsum' (analog sum of the sumouts, and proportional to the energy deposited) discriminated at 75 mv. A hadron calibration beam showed this trigger to be fully efficient at a hadron energy of 15 GeV, the energy at which cuts were made. The analysis is performed on events that have satisfied either the QUASI or PTH trigger, but the hadron energy cut of 15 GeV rejects events that satisfied only the QUASI trigger.

Off-the-shelf NIM electronics perform the triggering and associated fast

logic, while latches, ADC's, TDC's, and readout electronics are done with a mixture of custom made units and off-the-shelf CAMAC modules. A PDP-11 controlled the data acquisition, wrote events to tape, and performed online analysis.

3.2.3 Beamline Interface

Crucial to determining the total cross section is beam gating and monitoring. The beam gate (BG), mentioned earlier, was sent for gating the Lab C detector. In addition, a Lab C livetime gate was started at the arrival of the BG and ended either at the end of the BG or when an event was taken. The Lab C gate was sent upstream for gating the scalers from the beam monitors to determine the number of secondaries during the live interval preceding the interaction. The Fermilab Neutrino Department employed a MAC computer for beamline data acqusition which interfaced with the Lab C PDP-11 for storing magnet and gated information on tape.

CHAPTER IV. DATA ANALYSIS

To be included in the final event sample, an event must satisfy the following requirements: an analyzable muon originating from the vertex traversing the entire toroidal system, a vertex such that the energy from the hadron shower is fully contained in the calorimeter, and lower limits for the muon momentum and hadron energy.

An event which satisfies these requirements is shown in Figure 4.1. Note the three flash chamber views (U, Y, and X) which provide the high resolution of the shower and the exiting muon; the total number of flash chamber cells hit in all three views is given in the label HITTOT. In addition, a fit of the muon is shown, exhibiting the selection of hits in the toroid spectrometer used by the fitting program. On either side of the flash chambers are displayed the proportional planes. Each plane display indicates whether the channel has a 'hit bit' (to the left of the plane) and gives the analog pulse height (to the right of the plane) normalized to the maximum pulse height, specified in the label PHT: MAX. The label PHT also contains the sum of all the pulse heights (SUM) and the sum for which the hit bits were on (HBT). Each prop plane display also shows whether the plane produced an Analog Multiplicity (A) and/or a Single (S) signal.

The following sections discuss the techniques by which the events are analyzed and tested for the requirements discussed above.

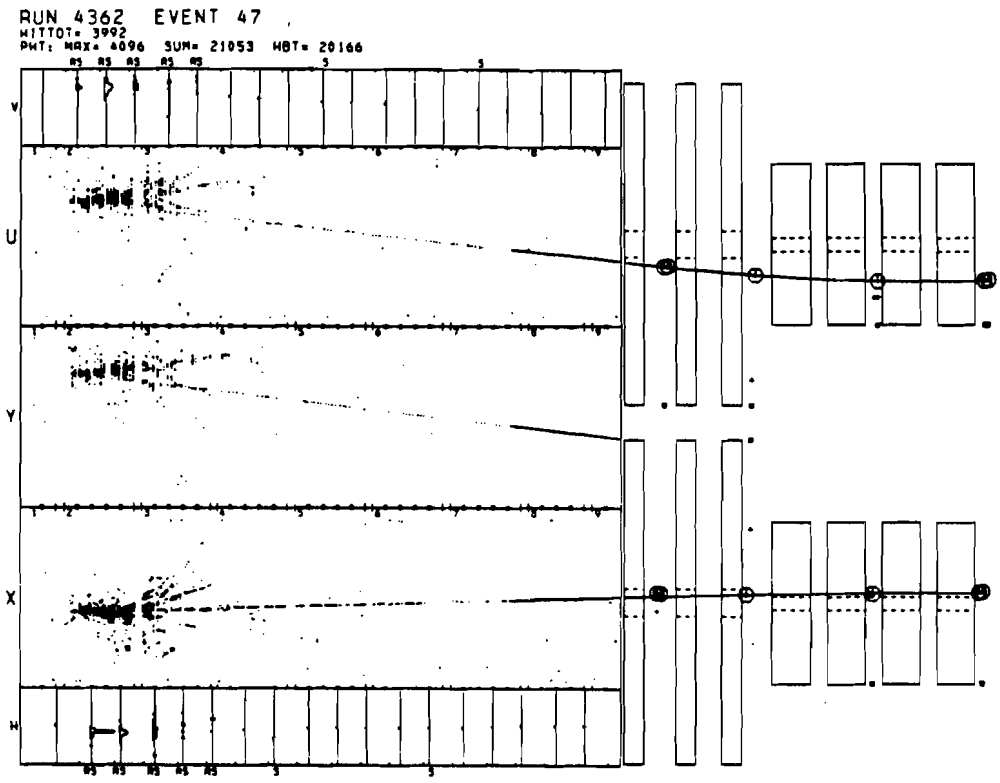

Figure 4.1. A charged current neutrino event selected for the final event sample.

4.1 Fiducial Volume Determination

The first step towards obtaining an event sample is to define the fiducial volume in which events will be selected. The fiducial volume must be large enough to accept as many events as possible in order to increase event statistics, but small enough such that the entire event is contained in the detector and the exiting muon is not hidden by the shower for an event near the end of the calorimeter.

A z (longitudinal) cut is made from chambers 5 to 392; chamber 5 is used to insure that the vertex is within the calorimeter and is not from some upstream interaction, and chamber 392 was determined from shower length distributions to ensure containment of the hadron shower. A radial cut of

140 cm about the center of the detector is also made. This was deemed safe for shower containment from my analysis and by an E594 memo[18], which explained that the amount of the hadron shower outside the edge of the detector for a given vertex is more a function of hadron shower angle than energy.

4.2 Alignment

In order to successfully track the muon from a charged current interaction into the toroid magnets, the entire detector must be aligned. This is broken into two procedures: first the flash chambers in the calorimeter are aligned, then the toroid proportional planes are aligned to the flash chambers.

Each flash chamber, as discussed earlier, is composed of three separate polypropylene panels. Each panel must be corrected for its own shift and rotation with respect to the beam axis. In addition, because the panels are not rigid they have a degree of curvature in them that must also be corrected for. Finally, because each flash chamber is read out by two amplifiers, the location of the hits relative to each amplifier must agree, hence one more correction. This procedure therefore requires fitting for ten parameters for each flash chamber. To accomplish this a sample of events was compiled composed of cosmic ray muons and calibration test beam muons. An iterative procedure is used where the residual for each panel is calculated, and the parameters are fit under the constraints of the three view match and the results of a survey of the flash chambers. This method yields an approximate 1 milliradian systematic error to local line fits of muons.

The toroid planes are then aligned using the flash chambers and muons from runs where the toroid magnets have been degaussed. The planes are only fit for shifts since the rotations are small and there is no curvature.

4.3 Event Scan

In order to assist in program development, event classification and vertex location, all events were scanned by professional Fermilab scanners. In the end, it turns out, computer analysis of the event gives results as good as the scan. Scan and program information are then combined to give the best results.

4.4 Vertex Location

To determine the slope and intercept of the exiting muon track, it is necessary to find the event vertex. An attempt is made to find the vertex from the shower; a description of this code is given below. This information is meshed with the scan information: if the code fails and there is only scan information then the scan is used; if the code succeeds and there is no scan information then the code results are used; if both exist then a combination of the two is used which produces the best U-X-Y flash chamber match.

The analysis code to determine the vertex performs in this way: the first plane in a string of proportional planes that have been latched on the event is found. A search is then made starting 32 flash chambers upstream to find the first occurence of a specified fraction of flash chambers hit — this determines the longitudinal postion of the vertex. A transverse histogram is then computed about this position to get a rough location of the vertex. A least squares fit is performed to the flash chamber hits to get a finer measure of the vertex. A final fit is then done by starting downstream in the shower and walking upstream, using a dynamic window for selecting hits, and fitting to these hits.

4.5 Charged Current Identification

There are two types of neutrino (muon) deep inelastic events — charged

current and neutral current — which are identified by the presence of a prompt muon exiting from the vertex, or a lack of one. It is the job of the pattern recognition program to separate these event types.

The code to determine the event type starts with a 'searchlight' scan — an angular histogram of the flash chamber hits about the vertex. The peak is determined, and further iterations are performed on this peak to find the precise exit angle from the vertex. A subsequent iteration is done to find the efficiency of the chambers along the muon trajectory, defined as the ratio of chambers having 1 or 2 hits to those having 0, 1, or 2 hits. The muon is then projected backward to the vertex to determine how close the track comes to the vertex, and the chamber efficiency is recomputed after deciding if the muon went outside the detector. If it is found that the muon did not go out the back of the calorimeter, then the stopping point is located.

Based on the number of flash chambers the track traverses, the efficiency of the track, the distance of the projected muon trajectory from the vertex, the number of back-to-back hits in the proportional planes in the toroidal magnets, and the exit or stopping location of the muon, the event is classified as a charged current or a neutral current. Confusion in the classification could arise for particles at large angles which exit the side of the detector, or very low energy particles which straggle and stop before exiting. In fact, these problems don't exist for this analysis because events are selected only if they have a momentum-analyzable muon track traversing the entire toroidal system. The code was run on 9540 Monte Carlo events, and misclassified events were scanned. After making the cuts used for this analysis, no misclassified events remained.

Muons can also be produced by decays of particles within the hadron shower, but if the muon vertex is not near the event vertex then the classifi-

cation code won't find the track. If the code does find the track, the energy of the muon acquired from the decay is too small to enable it to pass through all the magnets. Hence, non-prompt muons produce no background.

4.6 Hadron Shower Energy

To reconstruct the neutrino energy from a charged current event, half the problem is obtaining the energy of the hadron shower and the other half is obtaining the energy of the muon. The calculation of the shower energy is performed solely with the flash chambers.

To zeroth order, the energy calculated from the flash chambers is a linear function of the number of cells hit. However, higher energy showers cause a saturation, the efficiency of the chambers reduce the number of hits, and the multiplicity of the chambers increase the number of hits. These effects are accounted for in the following procedure. Each chamber is divided into 10-cell regions. For each region, the multiplicity μ and efficiency ϵ are calculated using a sample of many fitted muons according to the formulas

$$\mu = \frac{\text{number of hits in the region}}{\text{number of times } > 0 \text{ hits were found in the region}},$$

$$\epsilon = \frac{\text{number of times } > 0 \text{ hits were found in the region}}{\text{number of muon tracks in the region}}.$$

For a given event each region in each chamber is corrected using the multiplicity and efficiency for that region. The efficiency is a combination of statistical efficiency (approximately 80%) and mechanical efficiency (approximately 85%; arising from such things as defects in construction, etc.). The above correction is performed only when the efficiency is greater than 30%. About 2% of the regions have an efficiency less than 30%, and for these regions the adjacent good regions are averaged to yield a corrected hit count for the dead region. In addition, the energy loss in each scintillator is approximately the same as in one beam of the calorimeter, so that for each

scintillator the corrected number of hits in the upstream and downstream beams are averaged and summed with the other corrected hits. These corrected hits are then used to establish a calibration constant with a known value, for example from a calibration beam. The resolution of the hadron energy is given in Table 3.1.

4.7 Muon Momentum

To calculate the muon momentum from a charged current event, two routines have been developed. These routines are discussed in some detail in the Appendix, and from now on will be referred to as Methods 1 and 2.

In analyzing data, the following approach has been made. The momentum used for the event is determined using Method 2. If this routine fails for any reason then the result from Method 1 is used. This technique takes advantage of both Methods: the high efficiency of Method 2 is obtained, and the ability to fit muons using only the vertex when the muon track is indeterminate is performed by Method 1. The resolutions for the two muon classes are given in Table 3.1, and the reconstruction efficiency is given in Chapter VII.

CHAPTER V. NORMALIZATION

To obtain the total cross section it is necessary to know the number of neutrinos which struck the target and how many target nuclei there are: this is the subject of this chapter.

A tagged beam is extremely difficult for a neutrino experiment because of the extremely large secondary fluxes — approximately 10^{15} particles per second — needed to compensate for the tiny neutrino cross section. Instead, the number of neutrinos is found by first determining the number of secondary particles from the beam monitors. The number for each monitor is found separately, then averaged together. The number of secondaries and pressure curves from the Čerenkov counter are used to determine the beam composition, then combined with transport and decay Monte Carlos to find the number and distribution of neutrinos at Lab C. The number of target nuclei is found by knowing the weight and composition of the calorimeter.

The following sections now expand on this process. More detailed information can be found in an E594 memo[19].

5.1 Determination of the Secondary Flux by the Ion Chambers

As mentioned earlier, the ion chambers operate by producing a current which is a function of the flux of particles traversing the chamber. This current is then digitized and read out with the beamline computer. Mathe-

matically, the operation is

$$\text{ion chamber counts} = \int F(I(A(t)))\,dt,$$

where

$A(t)$ = Beam intensity as a function of time,
$I(A)$ = Current at input to ion chamber digitizer as a function of beam through the chamber,
$F(I)$ = Frequency out of a digitizer as a function of the input current,

and the total beam is

$$\text{total beam} = \int A(t)\,dt.$$

Therefore, to obtain the amount of beam in a spill it is necessary to calculate $A(t)$. Halfway through the run, logic was installed which crudely measured the shape of $A(t)$ for each spill. Independently, E701 (another neutrino experiment upstream of Lab C) used a beam shape parameterization developed by P. A. Rapidis[20] applied to all spills. These two methods roughly agree, so since measurements don't exist for the entire run, and for ease of comparison between the two experiments, the parameterization was used for $A(t)$. Since all that is measured is the ion chamber counts and the spill width, and the function for obtaining the counts from the beam shape is non-linear, then an iteration must be performed varying the amplitude of $A(t)$ until the correct number of counts is achieved.

In order to determine $F(I)$ the digitizers used were tested by injecting known currents and measuring the output frequencies. The results are shown in Figure 5.1. For some train settings during the run it appeared as if the chambers were 'saturating' due to the high particle flux. In fact, this behavior was due entirely to the nonlinearity of the digitizer response curve. For all train settings except -165 the digitizer used for each chamber is known; for -165 it is necessary to average the two 20 picocoulomb/count digitizers because it is not known which was used.

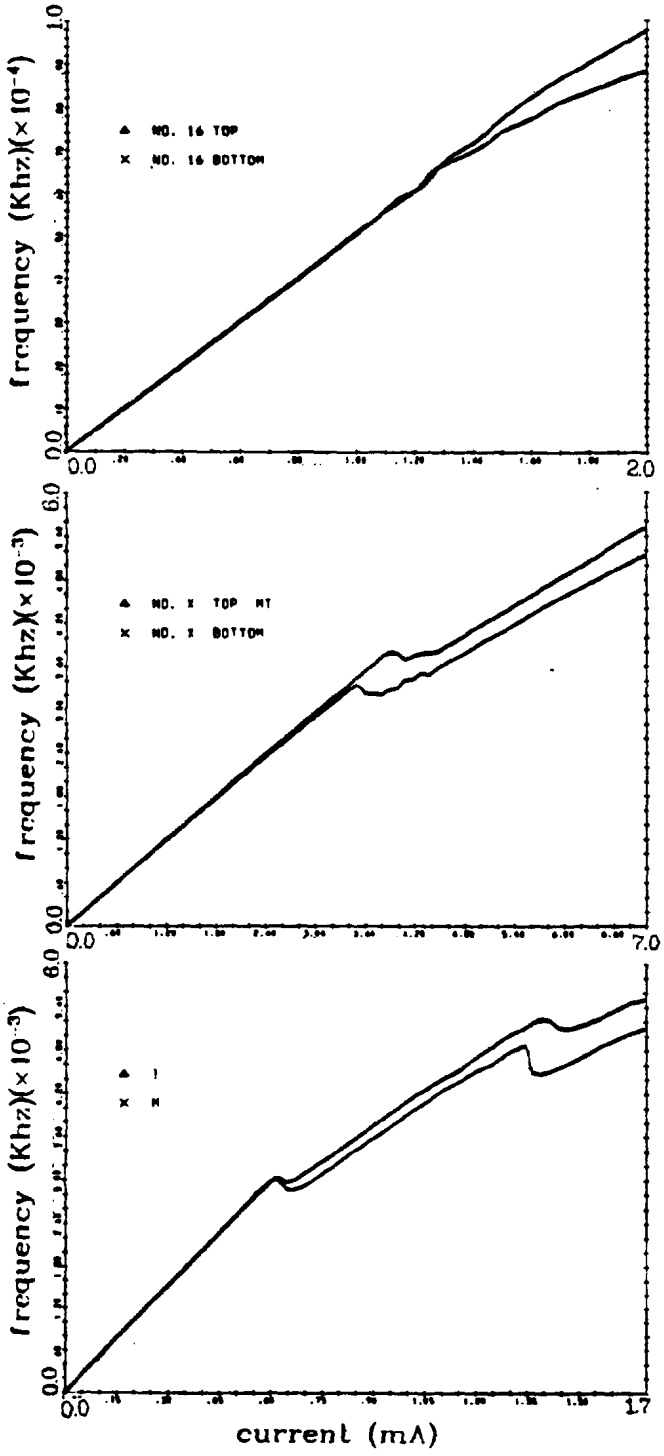

Figure 5.1. Calibration curves for the three digitizers used for the ion chambers. The top curve is the 20 picocoulomb digitizer, the middle curve is the 100 pc digitizer, and the lower curve is the 200 pc digitizer.

The quantity $I(A)$ was determined solely from the copper foil calibration run, discussed below.

Because the chamber constant, $I(A)$, is a function of the atmospheric pressure and temperature, these quantities need to be monitored. The digitized values from the chambers are corrected for pressure variations, but because of the location of the chambers the temperatures were stable and hence no temperature correction is necessary.

A much larger correction arises from the fact that the chambers respond differently to protons and mesons. A chamber was built and placed in the meson line at Fermilab by E616 (the predecessor to E701) to quantify the differences[21]. It was found that 8% more charge was deposited by protons than mesons. Since the ion chambers were calibrated with protons from the copper foil calibration, this leads to the correction given in Table 5.1. Figures 5.2–5.4 show histograms of the ratio of the ion chambers over the RF cavity for 0%, 8%, and 12% increases in the amount of charge produced by the protons in the beam (a train-dependent correction). 8% is used in this analysis, but may not be the ideal value to use for each chamber due to differences in the ion chambers construction. The 8% correction is used because each ion chamber has not been experimentally tested in the meson beamline to determine that the difference between train settings is due solely to the proton fraction difference. The largest correction occurs for the −165 train setting where the proton fraction is smallest. If an increase of 12% is used instead for this train setting a correction 4.3% smaller would occur. Since the analysis is performed by averaging the number of secondaries from the ion chambers with the number from the RF cavity, and since the RF cavity has a larger weight than the ion chambers in this average by a factor of 2, the number of neutrinos predicted would increase by approximately 1.4%.

train	*proton fraction*	*correction*
−165	*.012*	*.9210*
+165	*.666*	*.9733*
+200	*.782*	*.9826*
+250	*.909*	*.9927*

Table 5.1. Proton fractions and the corrections applied to the ion chambers for the four train setings.

Between each spill a test pulse of 0, 0.1, or 10 μA was injected into the digitizers for calibration purposes. However, even the 10 μA pulse was much too small to give a useful measurement of the calibration of the digitizer. But because of the good run-to-run stability of the test pulses they can be used as a relative correction to the digitizers — not yet done in full, however, because the correction has been found to be insignificant for a portion of the data.

Throughout the running the Čerenkov counter was periodically rolled into the secondary beam, and towards the end of the running a scintillator was installed in the Expansion Port. Secondaries produced from interactions in the Čerenkov counter and the scintillator increased the number of counts in the ion chambers downstream. This increase is corrected for by a scale factor.

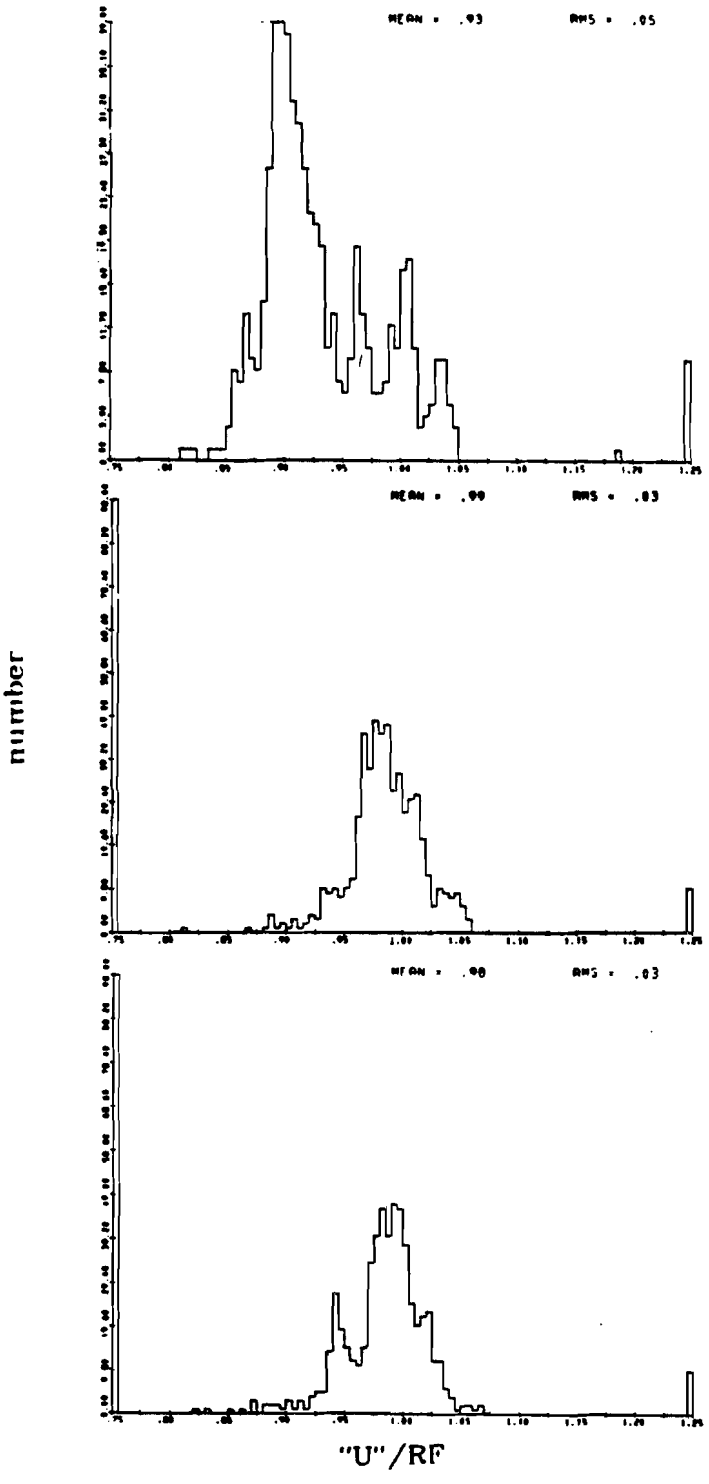

Figure 5.2. Ratios of the 'U' ion chamber output to the RF cavity output for various energy deposition corrections arising from the proton fraction of the beam. The top plot is 0% correction, the middle plot is 8% correction, and the bottom plot is 12% correction. The different peaks correspond to different train momenta.

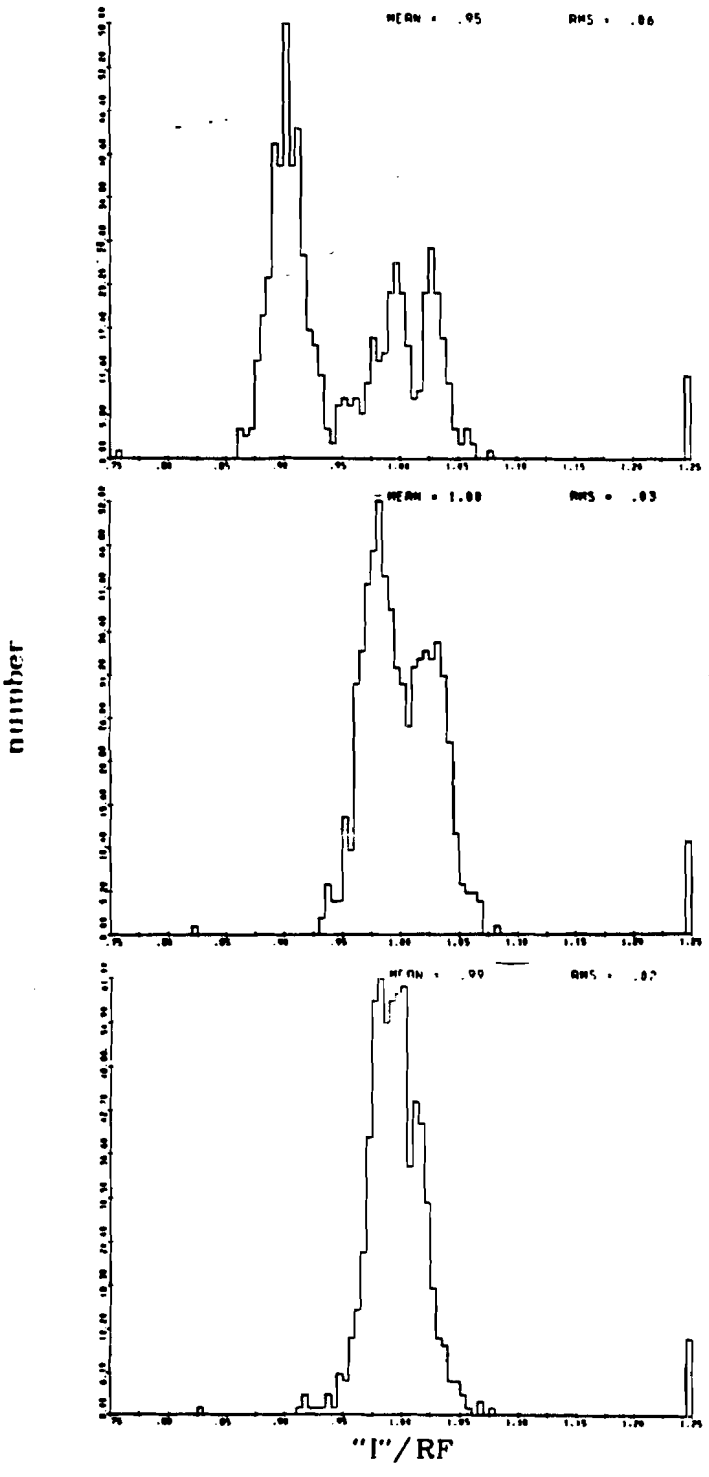

Figure 5.8. Ratios of the 'I' ion chamber output to the RF cavity output for various energy deposition corrections arising from the proton fraction of the beam. The top plot is 0% correction, the middle plot is 8% correction, and the bottom plot is 12% correction. The different peaks correspond to different train momenta.

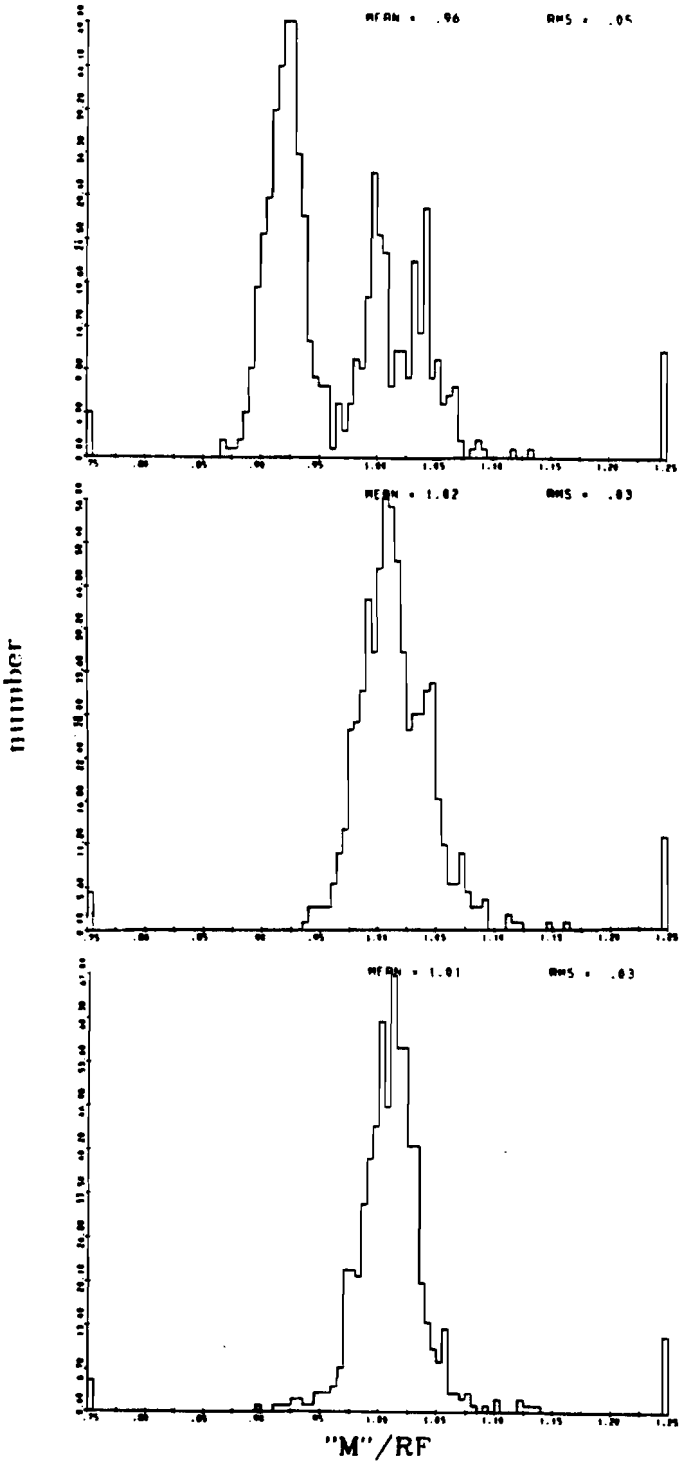

Figure 5.4. Ratios of the 'M' ion chamber output to the RF cavity output for various energy deposition corrections arising from the proton fraction of the beam. The top plot is 0% correction, the middle plot is 8% correction, and the bottom plot is 12% correction. The different peaks correspond to different train momenta.

5.2 Determination of the Secondary Flux by the RF Cavity

The RF cavity, as discussed earlier, produces a 53.1 Mhz RF voltage proportional to the beam current. Similar to the ion chambers, the voltage is digitized, scaled, and read out; mathematically

$$\text{RF counts} = \int F(V(A(t)))\,dt,$$

where

$A(t)$ = Beam intensity as a function of time,
$V(A)$ = Voltage at input to RF cavity digitizer as a function of beam through the chamber,
$F(V)$ = Frequency out of a digitizer as a function of the input voltage.

$A(t)$ was determined in the same manner as for the ion chambers, mentioned above.

A CAMAC-controlled attenuator accepts the output signal from the cavity so as to reduce the amplitude of the signal to a level acceptable to the following electronics. The $F(V)$ response of the RF cavity digitizer was measured at different attenuator settings, corrected to 0 db, and divided by the parameterization used, giving the results shown in Figure 5.5. The four low data points in the 0 db curve were taken upon retracing the curve, and do not indicate a measure of the point-to-point error. Agreement between the various attenuator settings is aproximately 2%.

There are two methods for determining $V(A)$: measuring the impedence of the cavity and the attenuation of the cables and attenuators[20], and from the copper foil calibration, discussed below. Results from these two methods differ by 5±3%. The mean value of these two methods is used for this cross section analysis.

A plot of ratios of the modelled beams, including E701's model for the RF cavity[20], is shown in Figure 5.6.

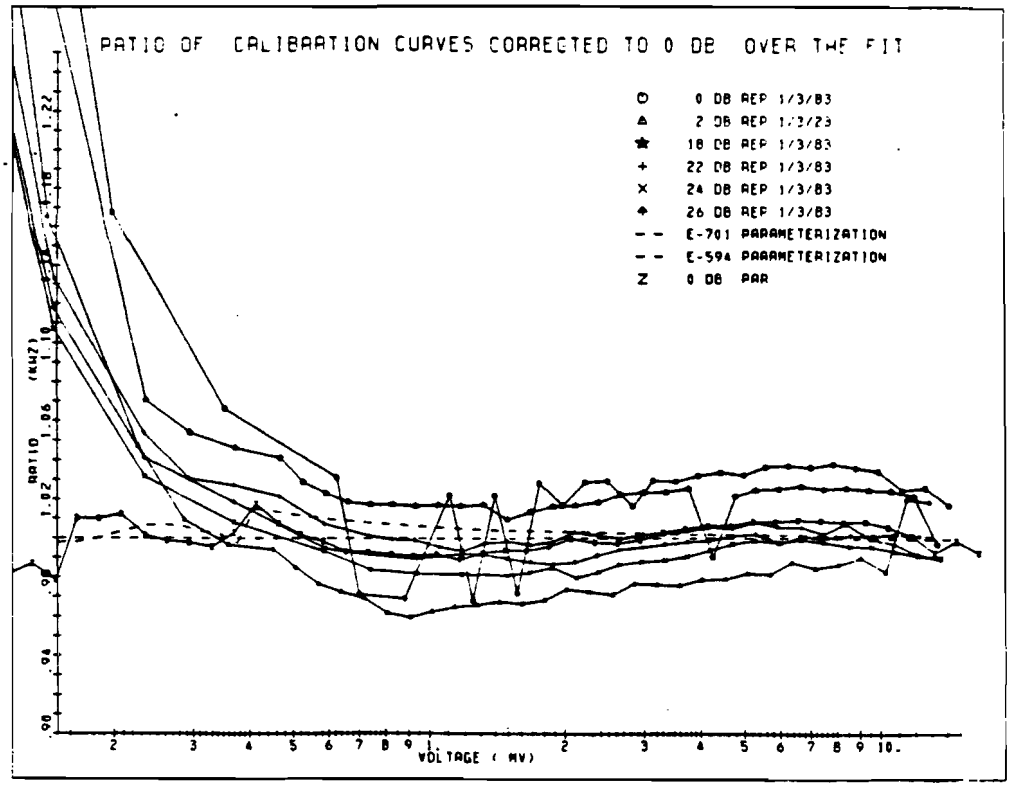

Figure 5.5. Calibration curves of the RF cavity digitizer corrected to 0 db for the various attenuator settings as measured by R. Pitt and P. Rapidis. Included are the parameterisations used by this experiment and experiment 701.

5.3 Foil Activation Calibration

To calibrate the monitors absolutely, a copper foil was put in the beam and irradiated with 200 GeV protons. The cross section for the transition to ^{24}Na has been measured to be $3.90 \pm .11$ mb for 400 GeV protons[22]. From the amount of ^{24}Na in the foil it was possible to determine the number of protons in the beam. The counts from the ion chambers and RF cavity were corrected for digitizer nonlinearities and added up, and a calibration constant was determined for each with an error of 5%.

A severe problem for the RF cavity modelling during the copper calibration is that the proton beam did not simulate the neutrino secondary beam.

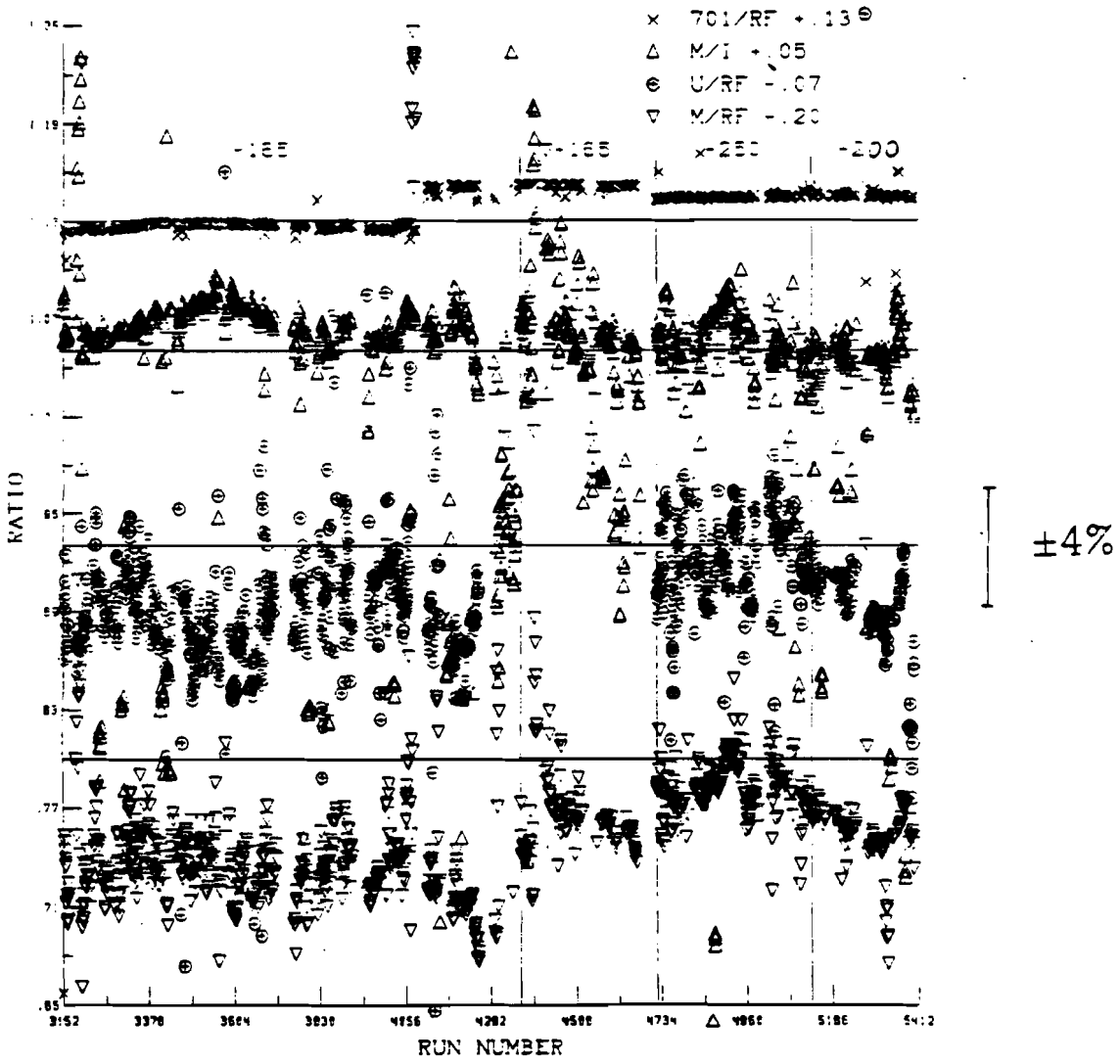

Figure 5.6. Ratios of the various corrected monitors as a function of run number, also labeled for each train. The upper ratio is the E701 RF cavity model over the E594 RF cavity model; the next ratio is the 'M' ion chamber over the 'I' ion chamber; the next is the 'U' ion chamber over the E594 RF cavity model; and the lower ratio is the 'M' ion chamber over the E594 RF cavity model. The ratios are offset for visual clarity.

The proton intensity was low, coupled with an attenuator setting that placed the number of counts very low on the $V(A)$ curves in the nonlinear region. In addition, the spill length is estimated to be at least 6 ms compared to 1.5 ms for neutrino running, and the shape is not known precisely, hence using $A(t)$

from neutrino running is an estimate. These problems are the major contributers to the 5% calibration difference of $V(A)$ between the measurements of the cavity and the copper foil calibration, mentioned above.

5.4 Čerenkov Counter

The Čerenkov counter, located on a moveable table with the RF cavity, was rolled into the beam for each train setting to determine the composition of the beam. The counter, shown in Figure 5.7, is an integrating counter because of the high particle flux. The counter was operated by varying the helium pressure for each accelerator cycle, thus changing the index of refraction. The Čerenkov angle changes with index, so as the pressure increases the light from different particle types reaches the phototube through the iris. A theoretical pressure curve for an ideal counter in an ideal beam is shown for a particle momentum of 100 GeV/c in Figure 5.8, and a curve taken during the +165 GeV train setting is shown in Figure 5.9. To unfold the momentum distribution of the secondaries it is necessary to Monte Carlo the beam through the train using TURTLE[23], a code written at Fermilab to model beam transport through user definable magnets and their locations, and to include other effects such as phototube efficiency, transition radiation, etc. Particle fractions determined for the runs used in the total cross section analysis are given in Table 5.2.

train	$\frac{e}{e+\pi(+\mu)}$	$\frac{\pi(+\mu)}{total}$	$\frac{k}{total}$	$\frac{p}{total}$
−165	*.031±.004*	*.900±.004*	*.059±.003*	*.012±.003*
+165	*.011±.003*	*.292±.003*	*.042±.002*	*.666±.006*
+200	*.006±.003*	*.189±.002*	*.0283±.0009*	*.782±.002*
+250	*.003±.002*	*.0775±.0015*	*.0135±.0006*	*.909±.002*

Table 5.2. Particle fractions at the expansion port for each train setting.

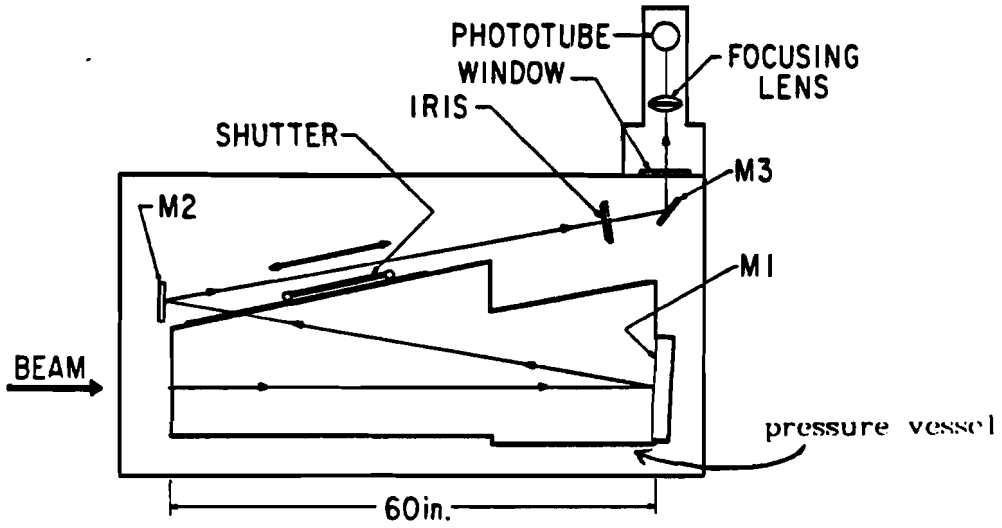

Figure 5.7. Čerenkov counter used for determining secondary beam composition.

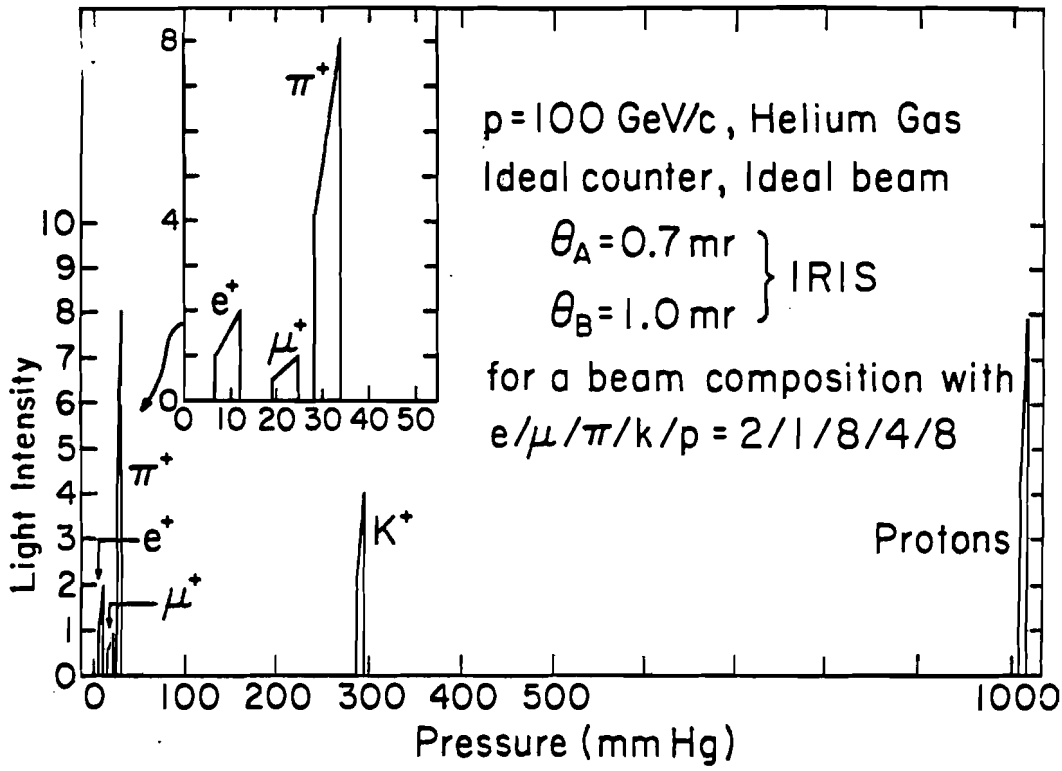

Figure 5.8. Theoretical pressure curves for an ideal Čerenkov counter. θ_A and θ_B are the lower and upper angles, respectively, with which the iris accepts light.

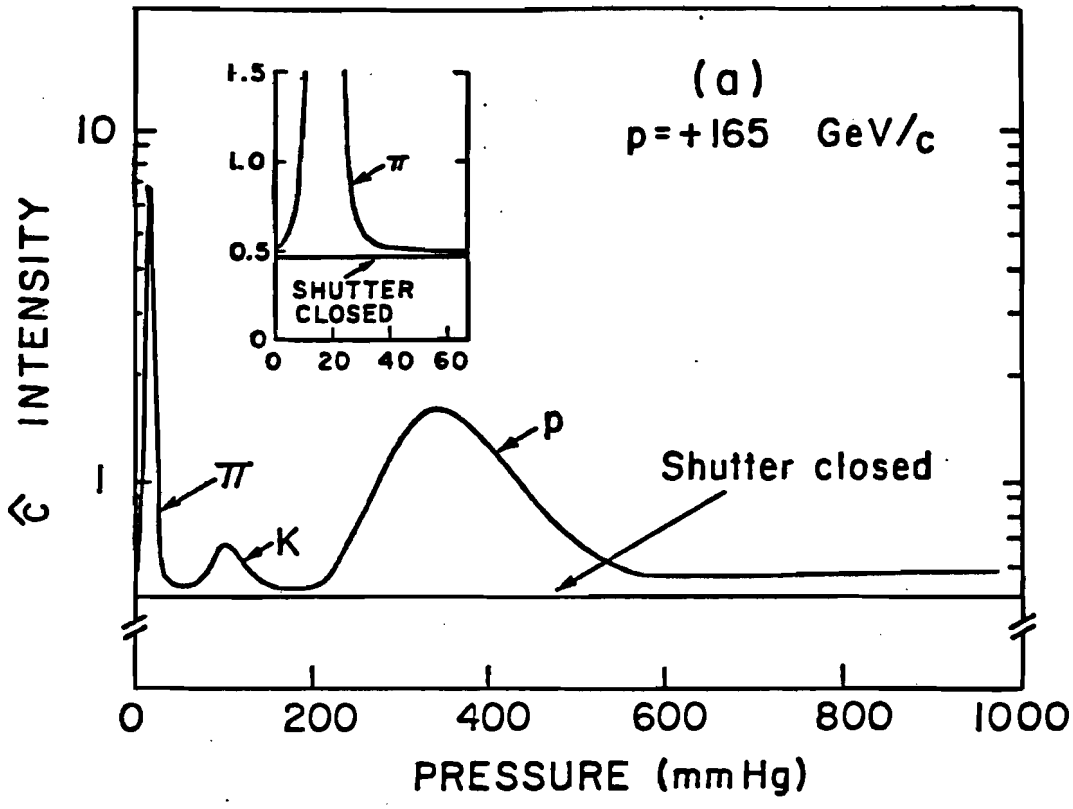

Figure 5.9. Čerenkov curve taken during the +165 running.

5.5 Monte Carlos

Given the number of secondaries it is then possible to calculate the number of neutrinos at Lab C. This is done with two Monte Carlos—one to transport the secondaries through the train given a production spectrum, and one to decay the secondaries.

TURTLE is run using the train magnet settings to produce particle location and momenta at the exit of the train. A beam Monte Carlo then takes these results and the π/K fractions from the Čerenkov results and decays the secondaries in the decay pipe. Projecting the neutrinos down the beamline gives the location and energy of the neutrinos at Lab C. This Monte Carlo also gives the number of neutrinos at Lab C given the total number of π's and K's.

5.6 Nucleon Number

The cross section is given for an isoscalar nucleus, hence it is necessary to know the number of target nuclei and their atomic numbers. The total calorimeter mass is determined in two ways:

1. Weigh as many beams (1/4 of a module — see Figure 3.9) as possible to get the average weight per beam, then multiply by the number of beams.
2. Weigh a piece of each component of the calorimeter, (flash chamber, proportional plane, etc.) determine from this the weight of the component, then sum up the weights from all the components.

Method 1 yields a mass of 330 ± 10 metric tons, while method 2 gives 331 ± 10, in excellent agreement.

Since the mass and composition of the individual components are known, the number of neutrons and protons in the calorimeter can be determined, and hence the N_N in Equation 2.19 known.

CHAPTER VI. EVENT MONTE CARLOS

In order to generate a Monte Carlo event, it is necessary to choose the kinematic quantities for the event. These are found by using a parameterization by Duke[24] of the structure functions. Using the beam Monte Carlo mentioned earlier to give the neutrino energy, a weight is determined for this event using the cross section formula. Events are then produced and selected depending on this weight, yielding values for x and y. From these two parameters the hadron and muon energies and angles are derived. The longitudinal location of the vertex is then placed randomly through the fiducial volume. The event can then be constructed by either a full shower simulation or a simpler four-vector method that generates four-vectors for the hadron and muon.

6.1 Full Shower Monte Carlo

This method takes the kinematics supplied and propagates the particles through the detector, simulating the response of the detector as accurately as is possible. Information returned from this process is packed into the same format as the data events so that the same analysis routines can be applied to the Monte Carlo as well as the data.

Problems limit the use of this method. It is slow, requiring much computer time for the generation and analysis of a single event. There is also a difficulty in simulating the energy of the hadron shower correctly. The current technique to obtain the hadron shower energy from the full shower

Monte Carlo is identical to that used in the four-vector described below — smear the thrown hadron energy according to the known resolutions.

There are benefits for creating a Monte Carlo of this type, however. Algorithms to be used for data analysis can be tested; for example neutral current-charged current separation can be studied since there is no question whether the event is a NC or a CC. Another major use of this Monte Carlo for this analysis is the determination of the muon momentum resolution for muons that pass near the toroid edges, discussed in Chapter 3.

A typical Monte Carlo event is shown in Figure 6.1.

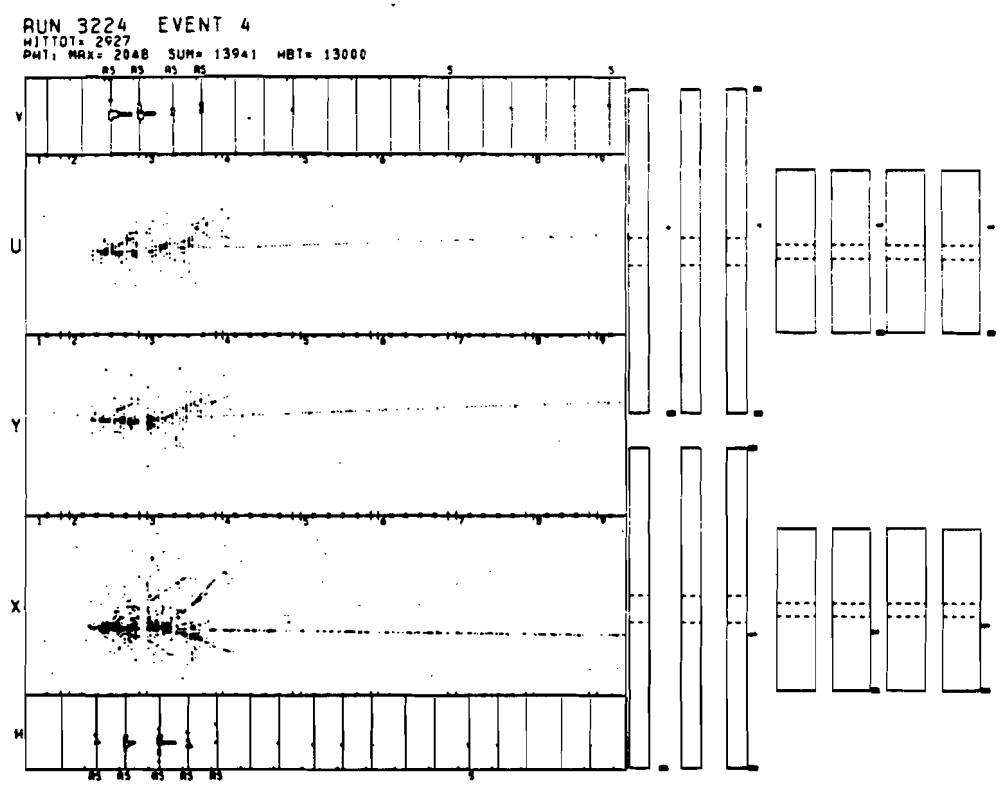

Figure 6.1. A typical Monte Carlo event.

6.2 Four-Vector Monte Carlo

A much faster method than the full shower Monte Carlo is to take the

exact kinematic quanties and smear them using the resolutions obtained in a calibration beam. The muon from the event is also propagated through the toroidal system in order to get the correct muon acceptance and muon 'trajectory type', a classification which is used to determine how much to smear the muon momentum (as mentioned above). This method proves to be as accurate as the shower Monte Carlo for this analysis, and is the one used for data comparisons.

To estimate the error contributed by the Duke structure function parameterization, the Monte Carlo is also run using structure functions determined from the simple power law discussed in Chapter 2, and from a parameterization by Buras and Gaemers[25], modified to agree better with the CDHS data[26].

Resolutions used for the four-vector Monte Carlo are shown in Table 3.1.

CHAPTER VII. BACKGROUNDS AND CORRECTIONS

7.1 Trigger Efficiency

As discussed in Chapter 3, the PTH trigger is a function of hadron energy deposited. The efficiency of this trigger can be determined from the hadron calibration beam: by triggering on hodoscopes set in the beamline the individual trigger components can be latched to determine efficiency. Using this method, Table 7.1 shows the combined trigger efficiency.

hadron energy (GeV)	*efficiency*
5	*.66±.07*
10	*.97±.01*
35	*.995±.003*

Table 7.1 Trigger efficiency.

7.2 Anti-counter Deadtime

The first detector component in the calorimeter is the 'anti counter', a liquid scintillator counter designed to veto the trigger on upstream interactions that reach the detector. The rate of the counter is monitored during the beam gate, and is approximately 20 khz. With a pulse width of 1 μsec, the counter produces a deadtime of about 2%.

7.3 Trigger Accidental Deadtime

The trigger, as explained earlier, requires the coincidence of a stretched AM, a stretched $\sum\sum 75$ and a delayed M to set the timing. If either the AM or the $\sum\sum 75$ is accidently triggered just before the real signal, then because of non-retriggerable hardware the signal disappears before the delayed M arrives. The AM and $\sum\sum 75$ rates outside of the beam are approximately 400 hz and 3500 hz, respectively, and their pulse widths are 1 μsec. This leads to a deadtime of less than 0.4%.

The AM and $\sum\sum 75$ rates used in the calculation above are expected to be similar to the rates during the beam by realizing that events occurring upstream will be accounted for by the A counter, and events occurring within the detector that are too low an energy to be triggered on will not produce these signals.

7.4 Classification And Reconstruction Efficiency

Events may be rejected from the final event sample due to misclassification and other problems in reconstructing the event. Table 7.2 gives event reconstruction efficiency statistics, based on a scan of a sample of rejected events.

	efficiency (%)	*68% CL (%)*
vertex location	*100*	*98.8*
cc identification	*100*	*99.6*
muon momentum determination	*100*	*99.7*
wrong sign muon rejection	*100*	*99.9*

Table 7.2 Event reconstruction efficiency determined from a sample of rejected events. No events were found to be rejected that should have been in the final event sample. An estimate of the efficiency is given at the 68% confidence level.

7.5 Cosmic Ray Background

The detector can be triggered during the neutrino spill by a cosmic ray muon or shower, and could possibly be classified and reconstructed as a neutrino event by the pattern recognition codes. However, because of the specific topology of the events in the event sample used, the number of cosmic rays entering this sample is exceedingly small. In fact, running the analysis routines on 4814 cosmic ray events results in only 1 event being called a charged current, and this event is cut out by requiring the muon to traverse the entire muon spectrometer. At the 90% confidence level, using the livetimes for the cosmic rays and for the *entire* Narrow Band run, at most 42 events are caused by cosmic rays.

7.6 Wide Band Background

Decays by secondary particles that have not been momentum selected by the train produce neutrinos at the detector that constitute a background to the momentum selected events. The number of wide band events is determined from a period of running where a collimator just downstream of the exit of the train is closed to stop all momentum selected secondaries. The number of events obtained during this running is too small to determine a spectrum, so the number of events is used to normalize a Monte Carlo distribution of wide band events using the Fermilab code NUADA[27]. The normalized spectrum is then put into the event generating Monte Carlo so that the wide band background correction is done with the acceptance correction.

Table 7.3 gives the number of wide band events during the closed collimator running after a 10 GeV hadron energy cut. A ratio is also made to the number of events predicted by Monte Carlo. Agreement is excellent for the positive train settings, but very poor for the −165 running. A search for

the cause of this discrepancy has been made without success. Keep in mind, however, that the background from wide band events is approximately .4% (after cuts), and although a 300% disagreement is alarming, the contribution to the event sample is small. Table 7.4 compares the number of events selected from the four trains for this analysis with the number of right-sign wide band background events predicted by Monte Carlo.

train	*events*	$\frac{\#\ data}{\#\ MC}$
−165	*66*	*3.07*
+165	*21*	*1.10*
+200	*12*	*1.16*
+250	*8*	*.87*

Table 7.3 Number of wide band background events, and the ratio to the number predicted by Monte Carlo.

train	*selected events*	*MC WBB*
−165	*1520*	*6*
+165	*2818*	*18*
+200	*2266*	*14*
+250	*2835*	*15*

Table 7.4 Number of selected events in the final event sample and the number of right-sign wide band background events predicted by Monte Carlo.

CHAPTER VIII. RESULTS

This chapter begins with a discussion of cuts made to arrive at the final event sample. Following are the total cross section results, along with a full explanation of the error treatment.

8.1 Event Rejection

To arrive at the final event sample used in the calculation of the total cross section, events must pass the pattern recognition and reconstruction codes. These events are then subject to further requirements to insure a clean and well understood sample.

Table 8.1 lists where events are lost for the four train settings in the compilation of the final event sample, starting with events satisfying either the QUASI or PTH triggers. The following is an explanation of the labels.

Beam monitor error. Before any further analysis is performed a check is made to ascertain that the beam monitors for this event contain trustworthy values. This includes scalers in the correct range, magnet currents on and at the right setting, etc.

Vertex rejection. The event has failed in the vertex routine to find a vertex. This is the step where the vast majority of non-neutrino events are rejected.

Outside fiducial volume. The vertex of the event fell outside the target volume specified.

	−165	+165	+200	+250
total triggers	*44240*	*33510*	*26356*	*34110*
beam monitor error	*7497*	*2127*	*2064*	*2541*
vertex rejection	*20512*	*7629*	*8483*	*13560*
outside fiducial volume	*8655*	*11836*	*7944*	*9308*
neutral current rejection	*2216*	*2899*	*1868*	*2088*
muon momentum failure	*454*	*1002*	*622*	*712*
muon class reject	*1094*	*2626*	*1663*	*1621*
insufficient iron cut	*482*	*539*	*366*	*451*
wrong sign muon	*18*	*5*	*6*	*17*
muon energy cut	*82*	*113*	*67*	*56*
hadron energy cut	*1710*	*1916*	*1007*	*921*
selected events	*1520*	*2818*	*2266*	*2835*

Table 8.1. Event rejection statistics for the four train settings used in this analysis.

Neutral current rejection. The event has been determined to be a neutral current.

Muon momentum failure. The muon analysis routines have failed in determining the momentum. The vast majority of rejections occur for muons exiting the side of the calorimeter and not entering the toroid magnets.

Muon class reject. The muon trajectory is not class '0' or '1', defined earlier; this requires that the muon, as determined by the fitting routine, passes through the entire muon spectrometer.

Insufficient iron cut. The fitted muon momentum often contains substantial errors when the muon oscillates through the bore of the toroid magnets. A possibility is to make cuts on the χ^2 and/or the $\frac{\Delta P}{P}$ of the fit, but a more accurate method is to simply require a minimum length of iron that the

muon must traverse, set to be the thickness of the three 24 ft toroid magnets and two of the four 12 ft magnets.

Wrong sign muon. The sign of the muon is the opposite of what it should be, and hence not the interaction desired.

Muon energy cut. The muon energy was below 15 GeV.

Hadron energy cut. The hadron shower energy was below 15 GeV.

The effect of the muon class, insufficient iron, muon energy, and hadron energy cuts are shown in the y and E_ν acceptances; see Figures 8.1 and 8.2.

8.2 Total Cross Sections

Tables 8.2–8.5 list the total cross sections for the four train settings. The errors have been broken down into statistical, systematic, and scale errors, where the scale error is independent of neutrino energy at a particular train setting, and the systematic error is everything other than the statistical or scale error. The binning has been chosen to center on the π and K peaks. The mean neutrino energy has been calculated using the neutrino flux from the beam Monte Carlo.

energy bin (GeV)	*mean neutrino energy (GeV)*	*cross section slope* ($\times 10^{-38} cm^2/GeV$)	*scale error*
30–55	*43.0*	$.294 \pm .016 \pm .026$	$\pm$ 4.50%
55–65	*59.7*	$.329 \pm .019 \pm .024$	
65–135	*78.3*	$.422 \pm .018 \pm .074$	
135–200	*150.9*	$.388 \pm .022 \pm .041$	

Table 8.2. Total cross section results for train −165. The first error is statistical, the second systematic.

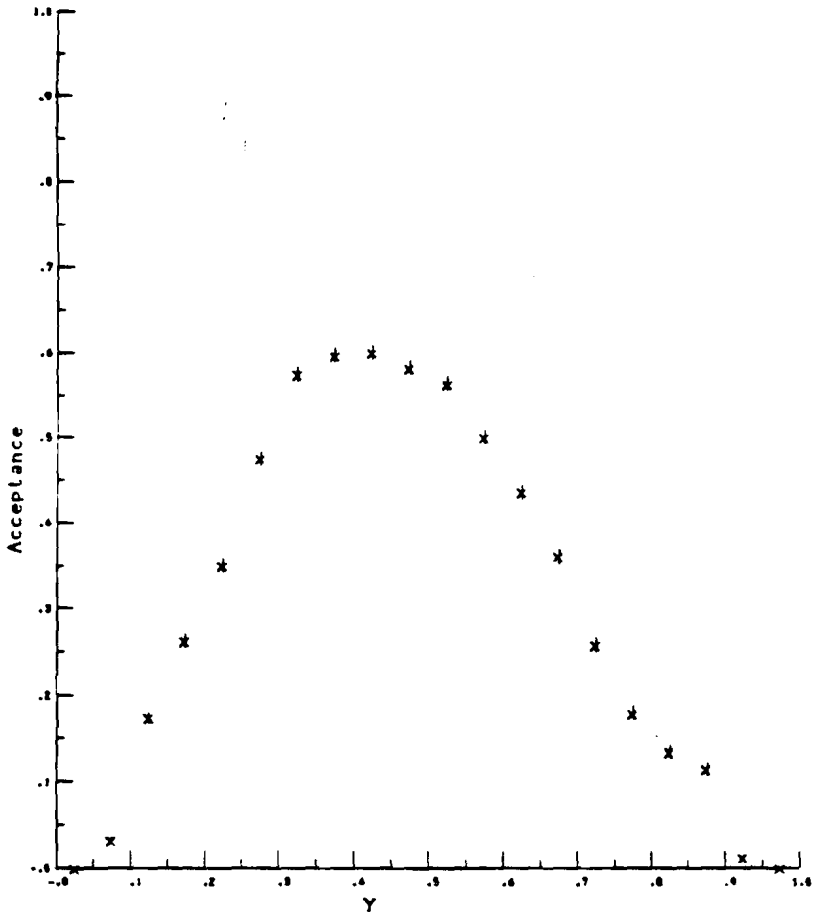

Figure 8.1. y **acceptance for train +165. The low acceptance at low** y **is due to the hadron energy cut; the low acceptance at high** y **is due to the cuts on muon class, insufficient iron, and muon energy. The maximum acceptance of** $\approx .6$ **is due to the overlap of these cuts.**

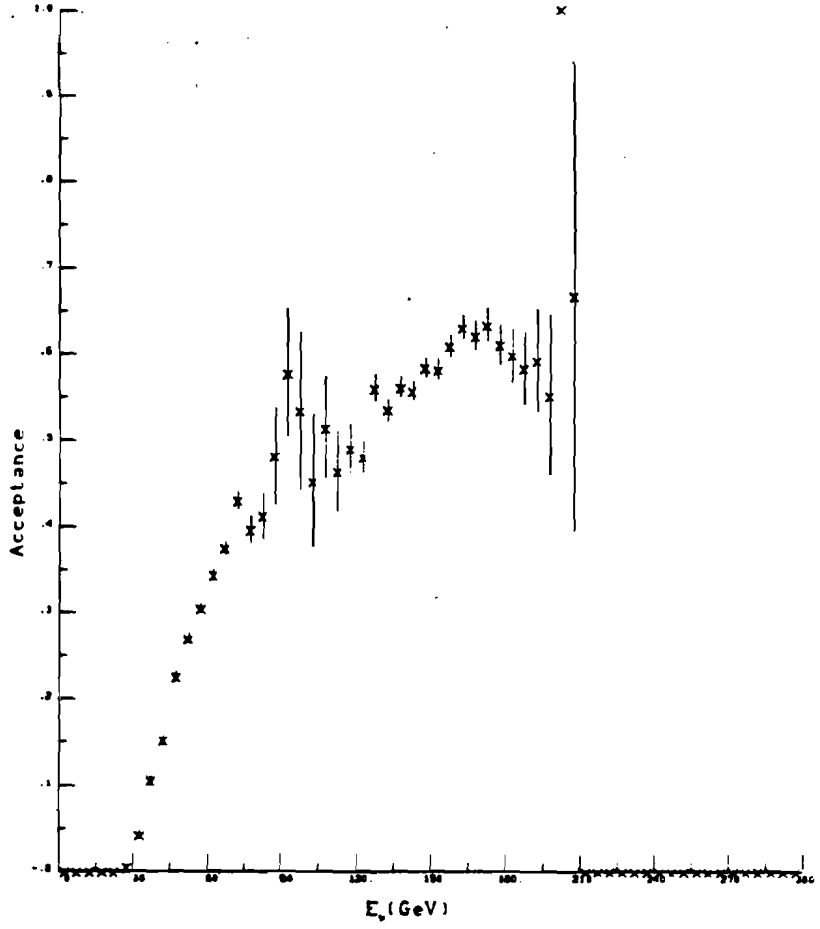

Figure 8.2. E_ν **acceptance for train +165. The region with the large errors around 100 GeV is the valley between the** π **and** K **peaks.**

energy bin (GeV)	*mean neutrino energy (GeV)*	*cross section slope* ($\times 10^{-38}$ *cm*^{2}*/GeV*)	*scale error*
40–80	*55.0*	$.659 \pm .018 \pm .071$	$\pm$ 4.78%
125–170	*145.8*	$.620 \pm .021 \pm .041$	

Table 8.3. Total cross section results for train +165. The bins have been chosen to center on the π and K peaks. The first error is statistical, the second systematic.

energy bin (GeV)	*mean neutrino energy (GeV)*	*cross section slope* ($\times 10^{-38}$ *cm*^{2}*/GeV*)	*scale error*
45–95	*64.4*	$.672 \pm .021 \pm .062$	$\pm$ 4.54%
140–215	*171.9*	$.630 \pm .021 \pm .045$	

Table 8.4. Total cross section results for train +200. The bins have been chosen to center on the π and K peaks. The first error is statistical, the second systematic.

energy bin (GeV)	*mean neutrino energy (GeV)*	*cross section slope* ($\times 10^{-38}$ *cm*^{2}*/GeV*)	*scale error*
50–115	*76.1*	$.589 \pm .018 \pm .048$	$\pm$ 4.45%
165–245	*202.1*	$.679 \pm .019 \pm .051$	

Table 8.5. Total cross section results for train +250. The bins have been chosen to center on the π and K peaks. The first error is statistical, the second systematic.

The combined cross section for the three positive trains is shown in Table 8.6. This is produced by weighting the three cross section slopes using the statistical errors and the errors that are train-dependent. The binning has been chosen to include the full range of neutrino energies from 30 GeV to 300 GeV. The results from this experiment compare well with the results from References 2–6, as shown in Figure 8.3.

energy bin (GeV)	*mean neutrino energy (GeV)*	*cross section slope* $(\times 10^{-38} cm^2/GeV)$	*scale error*
30–55	*42.9*	$.560 \pm .020 \pm .033$	$\pm$ 4.81%
55–65	*59.9*	$.580 \pm .021 \pm .026$	$\pm$ 4.64
65–85	*72.7*	$.607 \pm .018 \pm .033$	$\pm$ 5.06
85–120	*95.4*	$.717 \pm .024 \pm .055$	$\pm$ 4.65
120–150	*138.6*	$.595 \pm .021 \pm .029$	$\pm$ 4.77
150–180	*165.1*	$.608 \pm .018 \pm .031$	$\pm$ 4.77
180–210	*189.7*	$.688 \pm .021 \pm .052$	$\pm$ 4.43
210–300	*220.5*	$.678 \pm .024 \pm .036$	$\pm$ 4.53

Table 8.6. Combined total cross section results for trains +165, +200, and +250. The first error is statistical, the second systematic. The 'scale' error is not completely independent of energy due to the different scale error contributions from the different train settings. However, the scale error is highly correlated between energy bins.

From Tables 8.2 and 8.6 the mean cross section slopes and their χ^2's are calculated to be

$$(\sigma_T/E)_p = (.332 \pm .009 \pm .022) \times 10^{-38} \mathrm{cm}^2/\mathrm{GeV}$$

$$\chi^2/DF = 1.5, \qquad prob = 22\%$$

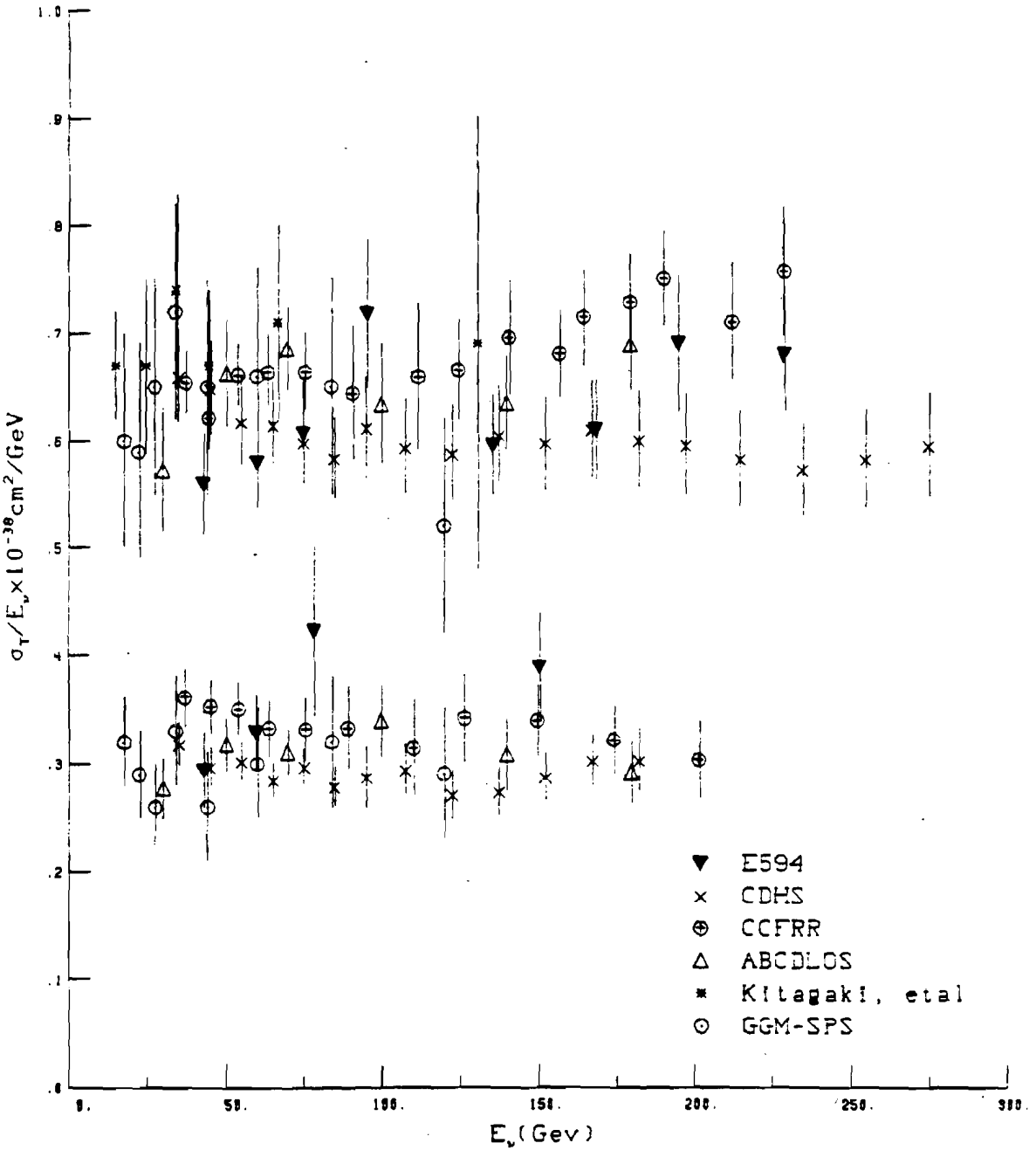

Figure 8.3. Total cross section results for this experiment compared with References 2–6. The error bars plotted contain the statistical, systematic, and scale errors.

$$(\sigma_T/E)_\nu = (.613 \pm .007 \pm .031) \times 10^{-38} \mathrm{cm}^2/\mathrm{GeV}$$

$$\chi^2/DF = 1.5, \qquad prob = 17\%$$

Where the first error is statistical, and the second error contains systematic and scale errors. As seen from the probabilities of the χ^2's, fitting the cross section slopes to constants is reasonably accurate. Comparing the cross section slopes with References 2 and 3:

Ref. 2 (CDHS):

$$(\sigma_T/E)_p = (.299 \pm .002 \pm .016) \times 10^{-38}\text{cm}^2/\text{GeV}$$

$$(\sigma_T/E)_\nu = (.609 \pm .002 \pm .041) \times 10^{-38}\text{cm}^2/\text{GeV}$$

Ref. 3 (CCFRR):

$$(\sigma_T/E)_p = (.340 \pm .003 \pm .020) \times 10^{-38}\text{cm}^2/\text{GeV}$$

$$(\sigma_T/E)_\nu = (.669 \pm .003 \pm .024) \times 10^{-38}\text{cm}^2/\text{GeV}$$

Note that both CDHS and CCFRR quote statistical errors that are much smaller than the results from this experiment. However, the dominant errors in the cross section measurements are the systematic and scale errors. Because the neutrino cross section in this analysis is calculated using the cross section measurements from three train settings, the combined systematic errors can be reduced even though some systematic errors are quite large, as mentioned below. Because CDHS had difficulties in the normalization of their cross section, their quoted scale errors of 5%–7.2% dominate in the errors quoted above.

8.3 Error Analysis

In expressing the error of the cross section, the error has been broken into a statistical error, a scale error (an error independent of neutrino energy at a particular train setting), and a systematic error (any error that is not a statistical or scale error). The systematic and scale errors are listed in Tables 8.7 and 8.8, along with the notation to be used in the following discussion and tables.

systematic error	*definition*
E1	*bin content error from hadron energy*
E2	*mean neutrino energy error*
E3	*wide band background error*
E4	*Monte Carlo statistical error*
E5	*Monte Carlo structure function error*
E6	$\pi \rightarrow \nu$ *acceptance error*
E7	$K_{\mu 2} \rightarrow \nu$ *acceptance error*
E8	$K_{\mu 3} \rightarrow \nu$ *acceptance error*
E9	π *fraction error*
E10	*K fraction error*

Table 8.7. Systematic error notation definitions.

scale error	*definition*
E11	*error from number of secondaries*
E12	*target nucleon number error*
E13	*isoscalar correction error*
E14	*reconstruction efficiency error*
E15	*other efficiencies error*

Table 8.8. Scale error notation definitions.

The error definitions in Tables 8.7 and 8.8 are self-explanatory, however a word should be said to make the definition of errors $E6$–$E8$ clearer. In Equation 2.19, the quantity $N_\nu(E_\nu)$ can be logically expanded to

$$N_\nu(E_\nu) = N_{sec}[f_\pi A_\pi(E_\nu) + f_K A_{K_{\mu 2}}(E_\nu) + f_K A_{K_{\mu 3}}(E_\nu)], \qquad (8.1)$$

where N_{sec} is the number of secondaries detected by the beam monitors, and f_π and f_K are the π and K fractions, respectively, of the secondaries. The quantities $A_\pi(E_\nu)$, $A_{K_{\mu 2}}(E_\nu)$, and $A_{K_{\mu 3}}(E_\nu)$ specifiy the number of neutrinos that enter the fiducial volume given a pion or kaon which might decay to a two-body final state, or a kaon which might decay to a three-body final state. It is the contribution to the cross section error from the errors of these three quantities that are represented by $E6$, $E7$, and $E8$.

Error $E2$ has been determined at the 68% confidence level by comparing the spectrum of muons from quasi-elastic interactions with the neutrino event energy spectrum from the beam Monte Carlo[28].

The systematic errors for the four trains are given in Tables 8.9–8.12, and the scale errors are given in Table 8.13.

energy	*systematic error (%)*									
bin (GeV)	*E1*	*E2*	*E3*	*E4*	*E5*	*E6*	*E7*	*E8*	*E9*	*E10*
30–55	*2.5*	*1.4*	*0.0*	*1.4*	*0.9*	*8.4*	*0.0*	*0.0*	*0.4*	*0.0*
55–65	*6.6*	*1.4*	*0.0*	*1.5*	*0.6*	*1.8*	*0.0*	*0.0*	*0.4*	*0.0*
65–135	*13.0*	*1.4*	*0.1*	*1.3*	*0.7*	*11.6*	*0.9*	*0.0*	*0.4*	*0.8*
135–200	*8.8*	*1.4*	*0.0*	*1.6*	*1.1*	*0.0*	*0.7*	*0.0*	*0.0*	*5.1*

Table 8.9. Systematic error contribution for train −165.

energy	systematic error (%)									
bin (GeV)	E1	E2	E3	E4	E5	E6	E7	E8	E9	E10
40–80	8.2	1.4	0.2	1.0	0.6	6.6	0.0	0.0	1.0	0.0
125–170	3.3	1.4	0.0	1.3	0.9	0.0	2.7	0.0	0.0	4.8

Table 8.10. Systematic error contribution for train +165.

energy	systematic error (%)									
bin (GeV)	E1	E2	E3	E4	E5	E6	E7	E8	E9	E10
45–95	5.1	1.4	0.2	1.1	1.0	7.3	0.0	0.0	1.1	0.0
140–215	4.7	1.4	0.0	1.1	0.6	0.0	4.0	0.0	0.0	3.2

Table 8.11. Systematic error contribution for train +200.

energy	systematic error (%)									
bin (GeV)	E1	E2	E3	E4	E5	E6	E7	E8	E9	E10
50–115	3.1	1.4	0.3	1.1	0.6	7.1	0.0	0.0	1.9	0.0
165–245	4.7	1.4	0.0	1.1	0.7	0.0	3.3	0.0	0.0	4.4

Table 8.12. Systematic error contribution for train +250.

	scale error (%)				
train	E11	E12	E13	E14	E15
−165	3.4	3.0	0.1	0.0	0.0
+165	3.7	3.0	0.1	0.0	0.0
+200	3.4	3.0	0.1	0.0	0.0
+250	3.3	3.0	0.1	0.0	0.0

Table 8.13. Scale error contribution for the four trains.

Tables 8.9–8.13 show that the error of the cross section measurement is dominated by $E1$, the bin content error arising from the uncertainty of the hadron energy, and $E6$, the $\pi \rightarrow \nu$ acceptance error. The following is a discussion of these errors.

Calibration of the calorimeter and muon spectrometer was intended to be accomplished through hadron and muon calibration beams. By varying the energy of the hadron beam, a function of the number of flash chamber cells hit versus energy deposited by the calibration beam can be determined, along with the energy resolution. Then during the neutrino running the number of cells hit within the hadron shower can be converted to an energy deposited. In a similar manner, by varying the momentum of the muon calibration beam the muon analysis codes can be checked for errors and the momentum resolution determined.

Unfortunately, problems have hampered this calibration. First, it is unknown whether a hadron beam accurately simulates the shower topology that is produced by a deep inelastic neutrino interaction. As discussed in the section on hadron energy determination, the energy calculated is dependent on the energy density of the event, hence an implicit assumption in the equivalence of the two types of showers is made.

And second, it has been observed that the mean number of hits in the flash chambers during the hadron calibration beam dropped continuously with each succesive event after the startup of a new tape. This effect occured because each calibration event was in the same location in the detector, and probably affected the magnetization of the magnetostrictive wand used in the readout of the flash chambers.

The muon calibration also had difficulties associated with it. As mentioned earlier, it has been found that muons passing near the edges of the

toroid magnets have a worse resolution, which is not yet understood. Unfortunately, because of the muon calibration beam location there was only one momentum setting where both types of muons occured.

In addition, because the beam location was fixed for most of the muon calibration run, it was not possible to attempt a measurement of the field as a function of position in the toroid magnets. As shown in Figure 3.11 and discussed earlier, the poor construction of the 24 foot diameter toroids leaves large errors in the understanding of the fields within the magnets.

There were runs taken with the muon calibration beam positioned in a spot different from the standard calibration location. However, this required that the muons pass through a wall of unknown composition of concrete and approximately one meter of iron before entering the detector. The necessary correction for this material reduced the accuracy of any measurement using these muons to an untrustworthy level.

It is believed that the muon momentum determination is better understood than that of the hadron energy. Accepting this belief, an attempt was made to determine the hadron energy calibration other than with the hadron calibration beam. A fit was made to the Monte Carlo y distribution using charged current events from the +165 running and fitting separately the neutrinos from π and K decays. The fit assumes the muon momentum is known accurately, and the hadron energy is the fit parameter, using sizeable low y and high y cuts to select good events. A calibration function for the hadron energy is then obtained. This function is related to the function obtained from the calibration beam by

$$E_{fit} = .0023E_{cal}^2 + .78E_{cal} + .43.$$

Figure 8.4 compares the two hadron energy distributions for the four train settings used in this analysis. The functions differ greatest at lowest energy,

and hence causes the greatest discrepancies at lower train settings, and especially for antineutrinos due to the y distribution being peaked at low y. This alternate calibration function has been used in the analysis to get a measure of the error of the hadron energy, and is represented by the notation $E1$ in the above tables.

Section 5.5 explains that the method used to produce a Monte Carlo neutrino distribution at Lab C employs TURTLE to obtain the four-momentum of particles emerging from the train.

An alternative to using TURTLE solely was developed by Carl Haber[29] of E701. During a portion of the neutrino running a hole collimator was scanned across the secondary beam in the Expansion Port. Using the spatial distribution produced in a downstream SWIC, a beam file similar to TURTLE was constructed by a Monte Carlo sampling of this distribution. Energies were determined for the rays produced in this manner by storing the energy for each ray from the TURTLE output in its particular horizontal, vertical, and angular bin, and then selecting the appropriate momentum for the ray for the new file.

There were a number of problems with this method. Primarily, there was considerable noise in the measured distributions. To correct for this a flat level was subtracted from each distribution. In addition, there was an overlap between adjacent positions of the collimator so that the profiles were not unique.

Because of the above problems, the TURTLE results were chosen to be used for the calculation of the total cross section. However, to get a measure of the error from TURTLE, the number of neutrinos at Lab C as predicted by TURTLE is compared to that predicted by Haber. This difference is represented by the notation $E6$, $E7$, and $E8$ in the above tables.

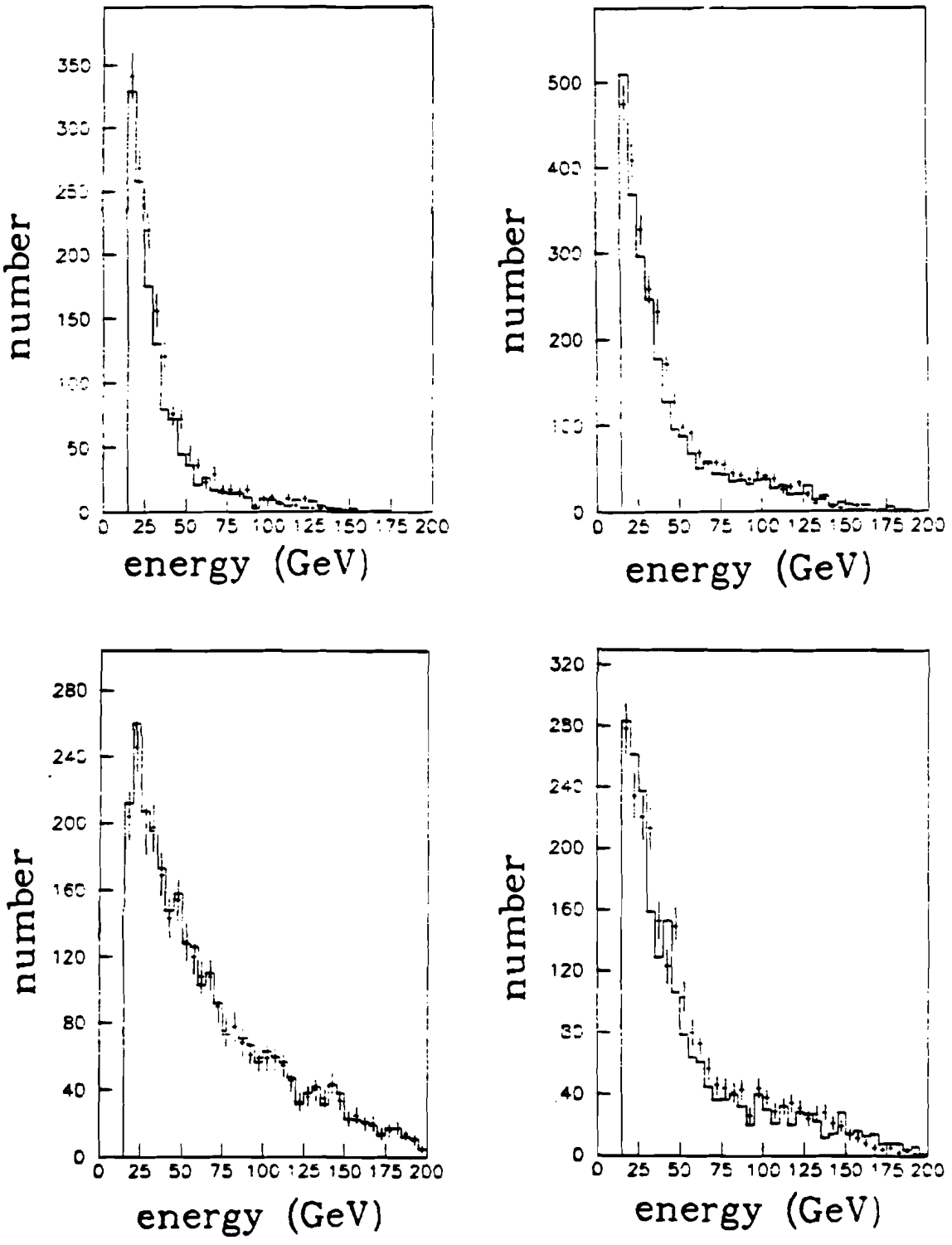

Figure 8.4. Hadron energy distributions for the four train settings. The individual points are obtained using the hadron energy calibration determined from the hadron beam, and the solid line is that determined from a fit to the y distribution. Clockwise from the upper left is train −165, +165, +200, and +250.

CHAPTER IX. CONCLUSION

This paper has discussed the various efforts that have gone into the measurements of the neutrino and antineutrino charged current total cross sections. The results of $(.332 \pm .009 \pm .022) \times 10^{-38}$ cm^2/GeV for the antineutrino cross section slope and $(.613 \pm .007 \pm .031) \times 10^{-38}$ cm^2/GeV for the neutrino cross section slope, where the first error is statistical and the second error contains systematic and scale errors, are consistent with previous measurements by other experiments.

Error calculations for the total cross section are difficult because most errors are partially correlated between energy bins or train settings. In addition, comparison of errors with other experiments is also difficult because of the lack of information on error analysis in the publications.

The discussion of the error treatment pointed out that the errors are dominated by the uncertainties of the energy calibration of the calorimeter and the beam divergence. Work is being conducted on both fronts in order to better understand these problems. Once these problems are solved the precision of the neutrino cross section measurement can be improved by as much as 8% and the antineutrino cross section by 25%. The fine quality of the monitor analysis has yielded results whose accuracy is very competitive with other experiments. Although there is a lack of statistics used for this analysis, understanding the energy calibration of the calorimeter may possibly lead to a loosening of cuts.

Appendix—Muon Analysis

A key quantity to be determined in this analysis for the total cross section is the energy of the exiting muon. The problem is straightforward, but difficult: complications from noise and inefficiencies at times mask the true muon path; 8- or 16-wire charge division implemented in the toroid proportional planes implies that delta rays have the ability to move the true location of a muon hit; and finite magnet size causes reconstruction difficulties at the magnet edges. To solve this problem two independent computer routines have been created. This appendix discusses these two routines and briefly the theory behind them.

A statement of the problem is as follows: A charged current neutrino interaction produces a muon which travels through the calorimeter into the toroid spectrometer. During its flight, the muon loses energy via dE/dx and bremstrahlung, and scatters by Gaussian multiple coulomb scattering (MCS), and possibly by a non-Gaussian hard scatter. There could also be delta rays produced by the interaction of the muon with the electrons in the medium. Travelling through the toroids the muon is deflected with a curvature inversely proportional to its momentum. Along the muon's path the detector planes locate the muon with a finite resolution and a degree of noise and inefficiency. Given these conditions, what is the momentum of the muon?

The important question concerns the muon momentum, but in finding

the momentum it is also possible to fit for other parameters, such as the slope and intercept of the muon in the calorimeter. Assume a fit will be made to find the parameters $p_1, p_2, , , p_n$, denoted as the vector:

$$\vec{p} = (p_1, p_2, \ldots, p_n). \tag{A1}$$

The goal is to find the minimum of the χ^2 surface with respect to these parameters, and what the parameters are at this minimum.

If it is assumed that measurements are uncorrelated, then the χ^2 function can be written as

$$\chi^2 = \sum_i^N \frac{(y_i - f_i(\vec{p}))^2}{\sigma_i^2}, \tag{A2}$$

where y_i are the detector measurements and $f_i(\vec{p})$ are the theoretical values. The σ_i^2 quantities are the errors in the y_i's.

However, multiple scattering by the muon produces correlations in the proportional plane hits due to deviations from the trajectory an unscattered muon would make. This yields a more complicated function:

$$\chi^2 = \sum_i^N \sum_j^N (y_i - f_i(\vec{p}))W_{ij}(y_j - f_j(\vec{p})). \tag{A3}$$

The matrix W_{ij} is called the weight matrix. The elements of the inverse of this matrix are defined by

$$W_{ij}^{-1} = \langle (y_i - f_i(\vec{p}))(y_j - f_j(\vec{p})) \rangle + \delta_{ij}\sigma_i^2{}_{\substack{\text{wire} \\ \text{resolution}}}. \tag{A4}$$

Note that in the case of uncorrelated errors the matrix and the function collapses to equation (A2). The elements of W_{ij}^{-1} can be simplified to a more understandable form:

$$W_{ij}^{-1} = \sum_n (z_i - z_n)(z_j - z_n)\theta_{\text{MCS}_n}^2 + \delta_{ij}\sigma_i^2{}_{\substack{\text{wire} \\ \text{resolution}}}, \tag{A5}$$

where the sum is over a sufficiently small integration step, and θ_{MCS_n} is the r.m.s. scattering angle at scattering point Z_n. Hence to find the quality of the fit the inverse weight matrix is calculated, inverted, and summed over the product of residuals to give the χ^2 . A measure of the error of a fit parameter is made by finding at what value of the parameter does the χ^2 increase by 1.

A.1 Method 1

This method[30] performs a fit for both the momentum and the muon trajectory in the calorimeter, a total of five parameters. A fit is first made for the muon at the end of the calorimeter, so as to reduce the effects of multiple coulomb scattering in the calorimeter and to get a good entrance angle to the toroids. Toroid hits are then manipulated so that back-to-back hits in the double sided toroid planes are combined to form one logical hit at the midpoint of the two wires with half the resolution error.

In this method the χ^2 equations have been linearized, hence there is an analytic solution. However, there is an error due to this linearization and the solution must be iterated. To start, the furthest downstream measurement is used to get an initial momentum based on the deviation of the track from a straight line. The track is projected using the calorimeter fit and the momentum determined. The χ^2 is calculated using correlated errors, and its position on the χ^2 surface predicts where the minimum ought to be. The parameters are recomputed to give this minimum, and the χ^2 is calculated again. This iterative procedure continues until the χ^2 converges, or until a specified number of iterations have been performed.

A.2 Method 2

A line fit is also made to the muon in the end of the calorimeter, but this fit is not a parameter in the fit of the χ^2 function. The track is projected

through the toroids at 10 GeV steps from 100 Gev defocused to 350 GeV focussed. At each step the χ^2 function is determined using uncorrelated errors for speed and containing hits that are within $3\sigma_{MCS}$ + 10cm of the projected muon trajectory. At the completion of this loop the momentum that used the most hits and had the lowest χ^2 is found. A similar loop is then done for ±5 GeV about this momentum using 1 GeV steps.

The full correlated χ^2 is then determined for seven momenta about the fine-stepping results. A parabola of χ^2 versus momentum^{-1} is fit to the results, and the momentum at the minimum is found.

A.3 Comparison

Each program treats the physics in a similar way: each contains a treatment of multiple coulomb scattering and ionization loss, but ignores the effects from bremstrahlung and hard scattering.

Execution time is also similar — approximately 1 second/event. However there are large fluctuations in the time for Method 2: a difficult event may cause the code to iterate through the correlated χ^2 fit many times due to irregularites in the parabolic shape. Also, Method 1 would be substantially faster if the calorimeter fit was removed as a parameter of the χ^2 fit.

The momentum resolution for both codes is also comparable. A muon calibration beam at 20, 40, 70, and 100 GeV yielded class '0' resolutions, defined earlier. Class '1' resolutions were obtained with Monte Carlo events. Resolutions used are given in Table 3.1; Tables A.1 and A.2 give the mean values and widths of Gaussian fits for the two codes for the calibration test beam. Included in these tables are the mean values of the estimates of the fit errors by the two codes. Note that Method 2 overestimates the errors – this is a consequence of the code assuming the fit in the calorimeter has no error.

calibration momentum	*number events*	*mean*	*sigma*	*⟨estimated sigma⟩*
22.3 GeV	*221*	*23.4*	*1.8*	*1.0*
44.0	*427*	*45.5*	*4.0*	*3.6*
76.8	*394*	*78.5*	*8.0*	*8.4*
108.5	*121*	*111.3*	*9.1*	*13.8*

Table A.1. Gaussian fit results from Method 1 for the muon calibration test beam.

calibration momentum	*number events*	*mean*	*sigma*	*⟨estimated sigma⟩*
22.3 GeV	*221*	*22.9*	*2.1*	*1.8*
44.0	*427*	*44.8*	*4.1*	*5.9*
76.8	*394*	*77.0*	*7.3*	*13.0*
108.5	*121*	*109.1*	*11.1*	*20.0*

Table A.2. Gaussian fit results from Method 2 for the muon calibration test beam.

The reconstruction efficiency of an event is different, however. Method 2 yields an efficiency of nearly 1 when given a good calorimeter muon road to start with. Method 1, however, has an efficiency of $< 100\%$ for the same conditions. This inefficiency is dependent on trajectory. As the muon begins crossing the magnet edges the code gets confused since a slight change in momentum gives a large change in trajectory, and hence χ^2 . Therefore many iterations do not result in a convergence of the χ^2 . Method 2 also get confused by magnet edges, resulting in a worsened resolution as does Method 1 for successful fits. The cause of the poor fits near the magnet edges is still not understood.

A benefit of the technique used by Method 1 is that a fit can be performed if the only calorimeter information of the muon is the vertex location; Method 2 must have a muon track. This is particularly helpful for events that are deep in the calorimeter and the muon is hidden by the hadron shower.

For neutrino data a fit-by-fit comparison of the two codes show Method 2 returning a 2% lower momentum at low momentum, but matching it at higher momenta. For calibration data the results are given in Table A.3.

calibration momentum	*number events*	$\frac{Method\ 2}{Method\ 1}$	$\sigma(\frac{Method\ 2}{Method\ 1})$
22.3 GeV	*221*	*.994*	*.012*
44.0	*427*	*.989*	*.013*
76.8	*394*	*.990*	*.027*
108.5	*121*	*1.002*	*.049*

Table A.3. A fit-by-fit comparison of the two muon momentum routines for four calibration momenta.

REFERENCES

1. For example, the discovery of the $W^{\pm}$ Intermediate Vector Boson by the UA1 collaboration: G. Arnison et. al., Phys. Lett. 134B, 469 (1984); and the UA2 collaboration: M. Banner et. al., Phys. Lett. 122B, 476 (1983).
2. H. Abramowicz et. al. (CDHS collaboration), Particles and Fields 17, 283 (1983).
3. R. Blair et. al. (CCFRR collaboration), Phys. Rev. Lett. 51, 343 (1983).
4. P. Bosetti et. al. (ABCDLOS collaboration), Phys. Lett. 110B, 167 (1982).
5. T. Kitagaki et. al., Phys. Rev. Lett. 49, 98 (1982).
6. J. Morfin et. al., Phys. Lett. 104B, 235 (1981).
7. Compare Reference 2 with Reference 3.
8. F. E. Close, "An Introduction to Quarks and Partons", Academic Press (1979).
9. G. Myatt, Proceedings of Neutrino 81.
10. Kuti and Weisskopf, Phys. Rev. D4 (1971) 3418.
11. Drell and Yan, Phys. Rev. Lett. 24 (1970) 181.
12. Brodsky and Farrar, Phys. Rev. D11 (1975) 1309.
13. de Groot, et. al., Z. Physik C1 (1979) 143.
14. Gross and Smith, Nucl. Phys. B14 (1969) 337.
15. D. Allasia et. al., Phys. Lett. 107B, 148 (1981),
16. D. Allasia et. al., NIKHEF-H/83-3 (1983).

17. POISSON is a code to solve Poisson's equation, written at CERN by Christoph Iselin, T604, CERN,LEP/TH.

18. J. A. Slate "The Edge of the E594 Fiducial Volume", E594/83-14 (1983).

19. R. E. Pitt "Current State of The E-594 Narrow Band Flux Analysis", E594/84-24 (1984).

20. K. Lang "RF Cavity Calibration", E701 memo, 4/30/83.

21. M. Purohit "Nucleon Structure Functions from ν_μ-Fe Interactions and a Study of the Valence Quark Distribution" (Thesis), CalTech (1984).

22. S. I. Baker, Nuc. Inst. & Meth. 222, 467 (1984).

23. D. Carey, "TURTLE (Trace Unlimited Rays Through Lumped Elements) A Computer Program For Simulating Charged Particle Beam Transport Systems", PM 9, (1978)

24. Duke and Owens, Phys. Rev. D30 (1984).

25. Buras and Gaemers, Nucl. Phys. B132 (1978) 249.

26. F. E. Taylor "Structure Function Fits and Constraints for the E-594 Monte Carlo", E594/84-2 (1984).

27. D. Carey and V. White, "NUADA The Fermilab Neutrino Flux Program", PM 0011, (1975)

28. J. Bofill "Upper Limit For ν_μ Oscillation Into ν_τ in a Dichromatic Beam" (Thesis), MIT (1984)

29. C. Haber "Neutrino Beam Monte Carlo for E-701", E-701 internal memo (1984); also Chapter 2 and sections 5.7-8 of Haber's thesis, Nevis Report R-1328.

30. L. Rosenson and R. Verdier "Charged Particle Tracking in Toroidal Magnetic Fields", E594/80-6 (1980).

ACKNOWLEDGEMENTS

To accomplish this thesis, there are many people that I feel a gratitude for, both professionally and personally.

My greatest thanks go to my advisor, Scott Whitaker. His perseverance at trying to keep me on the right track has been much appreciated. In addition, his ability and desire to tackle hardware, software, *and* physics problems provides for me a good model for which to compare myself in my own upcoming career. He is also always able to discuss the latest Celtics game (although he always roots for the wrong team).

A great deal of gratitude also goes to Randy Pitt. Working with Randy has taught me more than just the correct way to design electronics and code software. His research methods and the way he picks apart a problem until solved will always be a guide for my own work in the future. His typically careful and exhaustive work with the monitor data contributed significantly to an important area in the error analysis for the total cross section measurement. He also deserves a *large* amount of thanks for the effort he put into the correction of earlier drafts of this thesis. And I'm sure he didn't know the meaning of the word 'patience' until I came to Fermilab. But look at it this way: what better preparation for Brian?

Special thanks to Stu Fuess for his seemingly endless work on the alignment and hadron energy scale. His current role as the 'software czar' has made the analysis 'user friendly', and his coding should be a standard for all

programmers.

And special thanks to Maury Goodman, the previous 'software czar', for his work on the library, and for his tireless efforts at producing the best charged current-neutral current separation possible.

Thanks to Linda Stutte for the online software and for her work with NUADA and the wide band background problem.

Thanks also to Dan Owen and Harry Weerts for the excellent work on the Čerenkov analysis and the beam Monte Carlo, respectively. Their expertise gave me much confidence in their results in these crucial areas.

Thanks to Robin Verdier for his explanations and patience in the discussions of the muon momentum analysis routines.

Thanks to Frank Taylor and Tommy Lyons who are leaders in their respective arenas. While on opposite ends of the personality scale, both are able to accomplish the necessary tasks, and little would get done without them.

But a great big thanks go to my fellow graduate students: Juan, G.P., Tom, Mike, Aseet, and Rich from MIT, and Andy and John from MSU. *Much* was learned from these guys, and some *great* times were had. The influence they had upon me was great — I'll never forget them.

And of course to my friends at my home-away-from-home, the guys at CHC: Harry, Jim G., Dale, Cliff, Barry, Jim L., Dave, and all the others. It would have been nutso without these guys to 'weight' the other end of the scale.

And saving the best for last, my thanks to Kris for showing me that life does not revolve around high energy physics.